Retrieval of biomass combustion rates and totals from fire radiative power observations: Application to southern Africa using geostationary SEVIRI imagery

G. Roberts, M. J. Wooster, G. L. W. Perry,[1] and N. Drake
Department of Geography, Kings College London, London, UK

L.-M. Rebelo
Department of Geography, University College London, London, UK

F. Dipotso
Research Division, Department of Wildlife and National Parks, Kasane, Botswana

Received 24 March 2005; revised 1 July 2005; accepted 22 July 2005; published 12 November 2005.

[1] Southern African wildfires are a globally significant source of trace gases and aerosols. Estimates of southern African wildfire fuel consumption have varied from hundreds to thousands of teragrams (Tg), and better-constrained estimates are required to properly assess the effects of the pollutant emissions. A new approach for providing such estimates is via remote sensing observations of fire radiative power (FRP), a variable proportional to the rate of fuel consumption. The launch of the SEVIRI radiometer onboard the geostationary Meteosat-8 platform presents a unique opportunity to monitor FRP at 15-min intervals, allowing analysis of the complete diurnal cycle of biomass burning and calculation of the total fire radiative energy. Here we present the first FRP retrievals from SEVIRI and compare them to those derived from near-coincident MODIS overpasses. Strong agreement is achieved on a per-fire basis ($r^2 = 0.83$, $n = 139$, $p < 0.0001$), although at the regional scale SEVIRI typically underestimates FRP with respect to MODIS due primarily to its inability to confidently detect fire pixels with FRP $< \sim 100$ MW. Using relationships developed during ground-based experiments, SEVIRI-derived FRP measures are converted into estimates of the rate and total quantity of biomass combusted in southern Africa. During a 4.5 day monitoring period, and based on only the observed FRP recorded by SEVIRI, we infer that as a minimum estimate, peak combustion rates reached 50 tons/s and a total of 3.2 Tg of fuel was burnt in southern Africa. While provisional, we calculate that these figures maybe potentially increased upward by a factor of ~ 3 to account for atmospheric absorption of the upwelling radiation and for fires that were potentially cloud covered or too weakly emitting to be detected by the geostationary imager. The new tool of SEVIRI-derived FRP provides an insight into biomass burning on the African continent at a hitherto unobtainable temporal frequency, highly suited to the linking of pollutant emissions estimates to models of atmospheric transport.

Citation: Roberts, G., M. J. Wooster, G. L. W. Perry, N. Drake, L.-M. Rebelo, and F. Dipotso (2005), Retrieval of biomass combustion rates and totals from fire radiative power observations: Application to southern Africa using geostationary SEVIRI imagery, *J. Geophys. Res.*, *110*, D21111, doi:10.1029/2005JD006018.

1. Introduction

[2] Southern Africa represents a key region of savanna burning during the May to October local dry season, and it is estimated that this activity is responsible for between one fifteenth and one fifth of global wildfire emissions [*Andreae*, 1991; *Scholes et al.*, 1996]. These emissions modify the Earth's atmospheric chemistry and radiative budget in important ways that are not yet fully quantified and which depend in part upon the emissions' magnitude, spatial location, and timing [*Intergovernmental Panel on Climate Change* (*IPCC*), 2001]. Accurate emissions assessment requires reliable estimates of the amount of biomass combusted (M) and its annual and intra-annual variation [*Scholes et al.*, 1996]. Early combustion estimates were derived using aggregated fuel loads, combustion factors, and fire return intervals, varied as functions of biome type

[1] Also at School of Geography and Environmental Science, University of Auckland, Auckland, New Zealand.

0148-0227/05/2005JD006018$09.00

[*van der Werf et al.*, 2003]. Satellite remote sensing has been used to improve spatiotemporal sampling [e.g., *Swap et al.*, 2003], most typically by delineating burnt areas. Estimates of the amount of biomass combusted are then typically derived using [*Seiler and Crutzen*, 1980]

$$M = A \times B \times C, \tag{1}$$

where M is the amount of dry biomass combusted (kg m^{-2}), A is the burnt area (m^2), B is the fuel load (kg m^{-2}), and C is the combustion factor (unitless), which describes the fraction of the biomass exposed to a fire that is actually consumed (also termed "combustion efficiency").

[3] Unfortunately, while conceptually simple, the spatiotemporal variations of B and C in equation (1) are difficult to assess [*French et al.*, 2004], which has lead to increasing interest in alternative remote sensing approaches [*Andreae and Merlet*, 2001]. These include methods based around measurements of the thermal radiation emitted by burning, first to identify fires, and, second, to characterize key properties such as their rate of heat production/energy emission [*Riggan et al.*, 2004; *Wooster et al.*, 2004]. Remotely sensed active fire detection has a strong heritage [*Robinson*, 1991], and EO-derived data on fire occurrence have already been used to parameterize the lower boundary condition of emissions transport models [e.g., *Schultz*, 2002; *Reid et al.*, 2004; *Generoso et al.*, 2003]. Unfortunately, with the notable exception of the GOES satellite fire products [*Prins et al.*, 1998; *Prins and Menzel*, 1994], the limited overpass frequency of the polar-orbiting satellites typically used to supply active fire data, coupled with the strong diurnal variation in fire frequency, mean that the data obtained thus far generally represent only isolated temporal samples of the "true" fire activity level. Furthermore, this limited temporal sampling means such active fire data are generally provided at timescales inconsistent with the three-dimensional (3-D) modeling of atmospheric transport [*Moula et al.*, 1996; *Wittenberg et al.*, 1998]. The use of geostationary sensors typically increases temporal sampling frequency by an order of magnitude when compared to polar-orbiting satellites, and recent work by *Reid et al.* [2004] shows the predictive improvements gained by assimilating high temporal resolution geostationary fire detections into atmospheric aerosol transport models.

[4] Until now geostationary fire detection has been possible only with data from the GOES satellite series positioned over the Americas [*Prins et al.*, 1998]. However, the new Spinning Enhanced Visible and Infrared Imager (SEVIRI) on board the Meteosat-8 (formerly Meteosat Second Generation; MSG) satellite now offers this capability for Africa and Europe. Here we use SEVIRI to provide the first geostationary active fire observations over southern Africa during a key period of the 2003 dry season. In addition to fire detection, SEVIRI is used to provide information on the fire characteristics via measurement of the fire radiative power (FRP), a variable proportional to the rate of combustion and emissions production [*Kaufman et al.*, 1998b; *Wooster et al.*, 2004; 2005]. Integrating FRP observations over time provides a measure directly relatable to the amount of fuel biomass combusted. This physically based methodology is fundamentally different to that from which equation (1) is derived and represents the first attempt to derive semicontinental scale biomass burning rates and totals via an EO-based approach independent of the "traditional" *Seiler and Crutzen* [1980] method.

2. Fire Radiative Power

[5] Fire radiative power (FRP) is a measure of the radiant energy liberated per unit time from burning vegetation via the rapid oxidation of fuel carbon. FRP is therefore related to the rate of fuel combustion and carbon volatization. Temporal integration of FRP over a fire's lifetime provides a measure of the total Fire Radiative Energy (FRE), which is proportional to the fuel mass combusted and carbon volatized. *Kaufman et al.* [1996, 1998a] first estimated FRP from MODIS Airborne Simulator and polar orbiting EOS MODIS observations, and *Wooster et al.* [2003] detail the various methods available to derive FRP from EO data. The true FRP for a fire having temperature distribution T_n is provided by the Stefan-Bolzmann Law:

$$FRP = \varepsilon\sigma \sum_{i=1}^{n} A_n T_n^4, \tag{2}$$

where FRP is the Fire Radiative Power (J s^{-1} or W), σ is Stefan's constant (5.67×10^{-8} J s^{-1} m^{-2} K^{-4}), A_n is the area of the nth thermal component of the fire (m^2), T_n^4 is the temperature (K) of the nth thermal component and ε is the effective mean emissivity over all emitting wavelengths.

[6] Unfortunately, (2) is inappropriate for satellite image analysis since instrument spatial resolutions are inadequate for resolving the individual fire temperature components [*Riggan et al.*, 2004]. *Dozier* [1981] attempted to overcome this limitation by assuming a single subpixel homogeneous fire temperature and retrieving an estimate of this via bispectral (middle and thermal infrared; MIR and TIR) analysis. The retrieved fire temperature and subpixel area were then used to estimate FRP via (2), assuming $n = 1$. However, *Giglio and Kendall* [2001] show the bispectral method to be mostly inappropriate for use with low spatial resolution geostationary imagery, primarily because the increase in the TIR channel signal seen at active fire pixels is often small and difficult to separate from changes due to ambient background temperature variations. Spatial misregistration and unresolved emissivity and atmospheric transmission differences between the MIR and TIR channels introduce further uncertainty [*Giglio and Justice*, 2003]. In contrast to the difficulties that can be found when isolating a fire's TIR signal in low spatial resolution data, because of the very intense radiative emission of fires at MIR wavelengths the amount by which the MIR radiance of a fire pixel is increased above that of the ambient background is much easier to quantify. On the basis of analysis of Planck's Radiation Law and the Stefan-Boltzmann Law over the range of temperatures found in vegetation fires, *Wooster et al.* [2003] show in fact that the radiative power of a subpixel fire is linearly proportional to the MIR radiance increase of the pixel above that of the ambient background. This direct, single-wavelength relationship allows FRP to be derived from lower spatial resolution imagery such as that delivered by geostationary systems:

$$FRP_{MIR} = \frac{A_{samp}\sigma}{a}\left(L_{h,MIR} - L_{bk,MIR}\right), \tag{3}$$

where fires are assumed to radiate as gray bodies [*Langaas*, 1995], $L_{h,MIR}$ and $L_{bk,MIR}$ are the MIR radiances of the active fire and ambient background, respectively, A_{samp} is the pixel sampling area (a function of the view zenith angle, ϑ_v) and a is a constant based on the empirical best-fit between emitter temperature and MIR radiance using a power law approximation to the Planck function. See *Wooster et al.* [2003] for full details.

[7] While the FRP methodology offers many advantages, it is also important to stress some of the current uncertainties, which are in addition to those inherent in use of the MIR radiance method of FRP retrieval fully detailed by *Wooster et al.* [2003]. Two factors are likely to reduce satellite-measured FRP below that emitted by the fire, and these are as yet largely unquantified. The first concerns surface fires in forests, where an unknown amount of radiant energy maybe intercepted (scattered and absorbed) by the forest canopy. While the effect of forest canopy interception on radiant energy emissions has not been examined, *Pereira et al.* [2004] have investigated the detectability of understory burns in Miombo woodland based on optical detection of burn scars. They found that burn scar detection was insensitive to viewing and illumination geometry and, more importantly, to forest structure and density. *Fuller et al.* [1997] present similar findings, which they attribute to the high forest canopy transmittance. These findings suggest that the amount of thermally radiant energy from the fire that is intercepted by the canopy maybe quite small, in part because of the naturally low tree density in many savanna areas. Second, although atmospheric effects perturb MIR wavelength observations far less than those at shorter wavelengths, allowing FRP retrieval through even dense smoke plumes, the radiative impact of the absorptive black carbon released during combustion [*Kirkevag et al.*, 1999] has not yet been fully studied. Both these factors mean that satellite-derived FRP observations are likely to be minimum estimates of actual fire-emitted FRP.

[8] FRP data from the MODIS sensor are beginning to be used as a tool for investigating spatial and temporal patterns of fire intensity. Recently, for example, they were used to test the oft-repeated hypothesis that forest fires in the Russian boreal forest have significantly lower mean intensities than fires in the North American boreal region [*Wooster and Zhang*, 2003]. In the current study, for the first time, we use the FRP technique with geostationary satellite data to target southern Africa (0° to 32° latitude, 9° to 42° longitude), a region responsible for a significant proportion of global biomass burning emissions. From the observed FRP we derive minimum estimates of the peak rates and total amounts of biomass combusted and carbon volatized from these records and through preliminary analysis provide some indication of the possible upper limits.

3. SEVIRI Imaging Radiometer

[9] The first of the four operational SEVIRI instruments was launched on board the Meteosat-8 satellite on 28 August 2002 and represents a major advance when compared to the previous three-channel Meteosat imager. SEVIRI provides 10-bit radiometric imagery and atmospheric pseudo-sounding data of the Earth disk, centered on Africa and Europe, every 15 min. SEVIRI's full characteristics are detailed by *Aminou et al.* [1997] and *Schmetz et al.* [2002] and only those relating to fire applications will be considered here. SEVIRI records data in eleven spectral channels located between 0.6 μm and 14 μm at a spatial sampling distance of 3 km at the subsatellite point (SSP), with a further high spatial resolution visible (HRV; 0.4–1.1 μm) broadband channel sampled at 1 km at the SSP. The instantaneous field of view (IFOV) of the narrowband channels is 4.8 km, while that of the HRV channel is 2.0 × 2.7 km (east-west and north-south, respectively). Interchannel spatial registration is better, 0.73 km, and geometric accuracy is within 3 km absolute and 1.2 km relative for all channels [*Aminou et al.*, 1997] (http://www.eumetsat.de/en/area2/proceedings/eump40/index.html). SEVIRI possesses channels at 10.8 μm (TIR) and 3.9 μm (MIR), allowing pixels containing fires down to a subpixel fractional area of between 10^{-3} to 10^{-4} to be detected, depending on the fire temperature [*Wooster et al.*, 2003]. Owing to equation (3) being based on a relative fire pixel radiance measure, it is the low noise of the MIR channel that is most important for FRP derivation (NEdT < 0.35 K @ 300 K). However, SEVIRI's onboard calibration system also delivers high absolute radiometric accuracy from geostationary orbit (exceeding 1 K).

[10] Two parameters fundamental to a sensor's ability to detect and characterize fires are the minimum detectable fire size and the related minimum measurable FRP, and the maximum fire size and FRP observable without sensor saturation. These parameters are primarily controlled by the sensor's MIR channel saturation temperature, IFOV, and spectral response function. SEVIRI's MIR channel was designed to saturate at ~335–336 K, similar to that of the AVHRR which is widely used for active fire detection [e.g., *Scholes et al.*, 1996; *Boles and Verbyla*, 1999; *Fraser et al.*, 2000; *Wooster and Strub*, 2002]. However, while AVHRR can detect active fires down to an area of around 100 m^2 at nadir, its MIR channel saturates over even relatively modestly sized fires (~1000 m^2), greatly hindering its use in fire characterization [*Robinson*, 1991]. The SEVIRI MIR channel is centered at a slightly longer wavelength than that of AVHRR, and since the intensity of solar reflected radiation falls markedly with increasing MIR wavelength, this aids the ability of SEVIRI to detect and characterize fires. Furthermore, the ground-projected area of SEVIRI's IFOV is more than an order of magnitude greater than that of AVHRR, allowing SEVIRI to measure the unsaturated MIR radiance of very much larger fires. SEVIRI's disadvantage is that it cannot distinguish fires as small or as weakly burning as those detectable by the AVHRR. Radiative transfer modeling suggests that SEVIRI should be able to detect and characterize fires whose FRP ranges from ~100 to ~1000 MW per pixel (Figure 1). By definition, the small or weakly burning fires that maybe missed by SEVIRI will each have low FRP and will each consume far less fuel per unit time than will larger, more detectable events. Thus the absolute importance of these "missed" fires depends on their frequency with respect to those of the more intensely burning and/or larger fires.

4. Fire Detection, Characterization, and Accuracy Assessment

[11] We investigated the fire detection and characterization capabilities of SEVIRI using 4.5 days of level 1.5

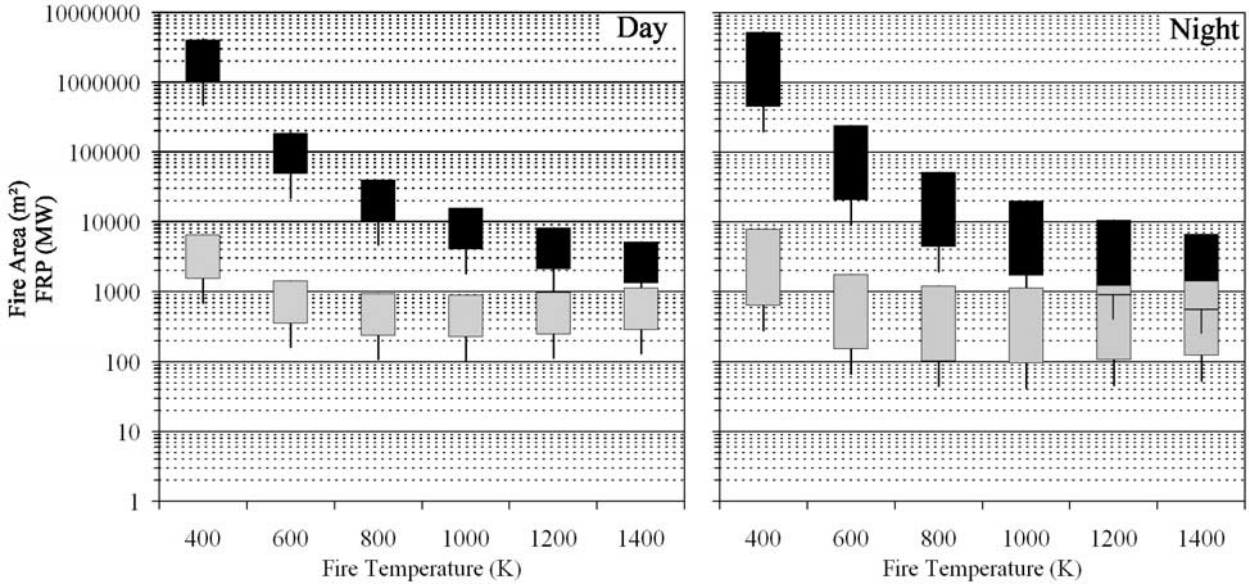

Figure 1. Estimated minimum subpixel fire area and FRP detectable using SEVIRI, and the fire area and FRP that would saturate the SEVIRI's MIR channel, both calculated over a 400–1400 K fire temperature range. Minimum detectable fire area is shown by the lower limit of the black bar, calculated as that which raises the MIR brightness temperature 12 K above that of the nonfire background. The vertical line extending below the bar shows the minimum detectable fire area if this threshold is reduced to 6 K. The fire area that saturates the sensor is shown by the upper limit of the black bar. FRP is represented by the grey bar and is calculated in each case by parameterizing the Stefan-Boltzmann Law with the relevant fire temperature and area. FRP is less variable since the two input parameters are inversely related. Calculations were performed using the MODTRAN radiative transfer code [*Berk et al.*, 1999] and assume a midlatitude summer atmosphere (rural aerosol, 23 km visibility), with a fixed surface reflectance (0.15) and surface emissivity (0.85) and a daytime solar zenith angle of 20°. Results differ between day and night due to differing assumed ambient background temperatures (day: 300 K, night: 285 K) and the lack of a solar reflected radiation contribution in the latter case.

imagery collected between 3 and 7 September 2003 (1200 to 2357 UTC, respectively), a total of 432 images. These represent the first dry-season data available for southern Africa and correspond to the end of the 16-month Meteosat-8 commissioning phase. Data were radiometrically and geometrically corrected by EUMETSAT and their quality is comparable to that of postcommissioning data obtained from January 2004 onward. Meteorologic cloud generally masks active fires from the sensors view, and so EO-derived active fire statistics are sometimes presented adjusted for the proportion of the land surface that was cloud free at the time of imaging [e.g., *Giglio et al.*, 2003a, 2003b]. Therefore before further analysis, each SEVIRI image had cloud-contaminated pixels detected and masked using a series of "cloud screening" tests based on the solar and thermal channel thresholding procedures of *Sauders and Kriebel* [1988], adjusted for southern African conditions.

4.1. Fire Detection

[12] The intense MIR energy emission from burning vegetation causes the MIR brightness temperature of SEVIRI pixels containing subpixel active fires to increase above both the colocated TIR channel measure and the surrounding MIR "nonfire" ambient pixels (Figure 2). On the basis of this divergence, two main categories of automated fire detection algorithm have been proposed, using either fixed or contextually varying thresholds. The former [e.g., *Arino et al.*, 1993] proceed on a per-pixel basis using a set of static thresholds, while the latter incorporate both absolute and relative thresholds that vary according to statistics derived from neighboring ambient background pixels [e.g., *Giglio et al.*, 2003a, 2003b]. *Giglio et al.* [1999] and *Ichoku et al.* [2003] provide detailed reviews of the fixed and contextual approaches, concluding that contextual methods show significant performance improvements with regard to their ability to adapt to changing environmental and scene conditions. Geostationary data is best analyzed using a contextual approach since a wide range of bioclimatic conditions and Sun-Earth-sensor geometries can be present within a single scene. *Prins et al.* [1998] previously adopted a contextual fire detection approach for use with GOES.

[13] The fire detection algorithm developed for SEVIRI is based on that used to generate the MOD14 fire products from MODIS infrared radiance observations [*Justice et al.*, 2002]. The MODIS fire pixel detection algorithm has been developed to be globally applicable [*Kaufman et al.*, 1998b; *Giglio et al.*, 2003a, 2003b], and some adjustments were made to optimize its performance when applied to SEVIRI data of southern Africa. SEVIRI data can contain much larger intrascene solar zenith angle and ambient background temperature variations than is generally the case with MODIS, and, as a result, the absolute and contextual thresholds used in the original MODIS-optimized algorithm required adjustment. Optimization was performed by allow-

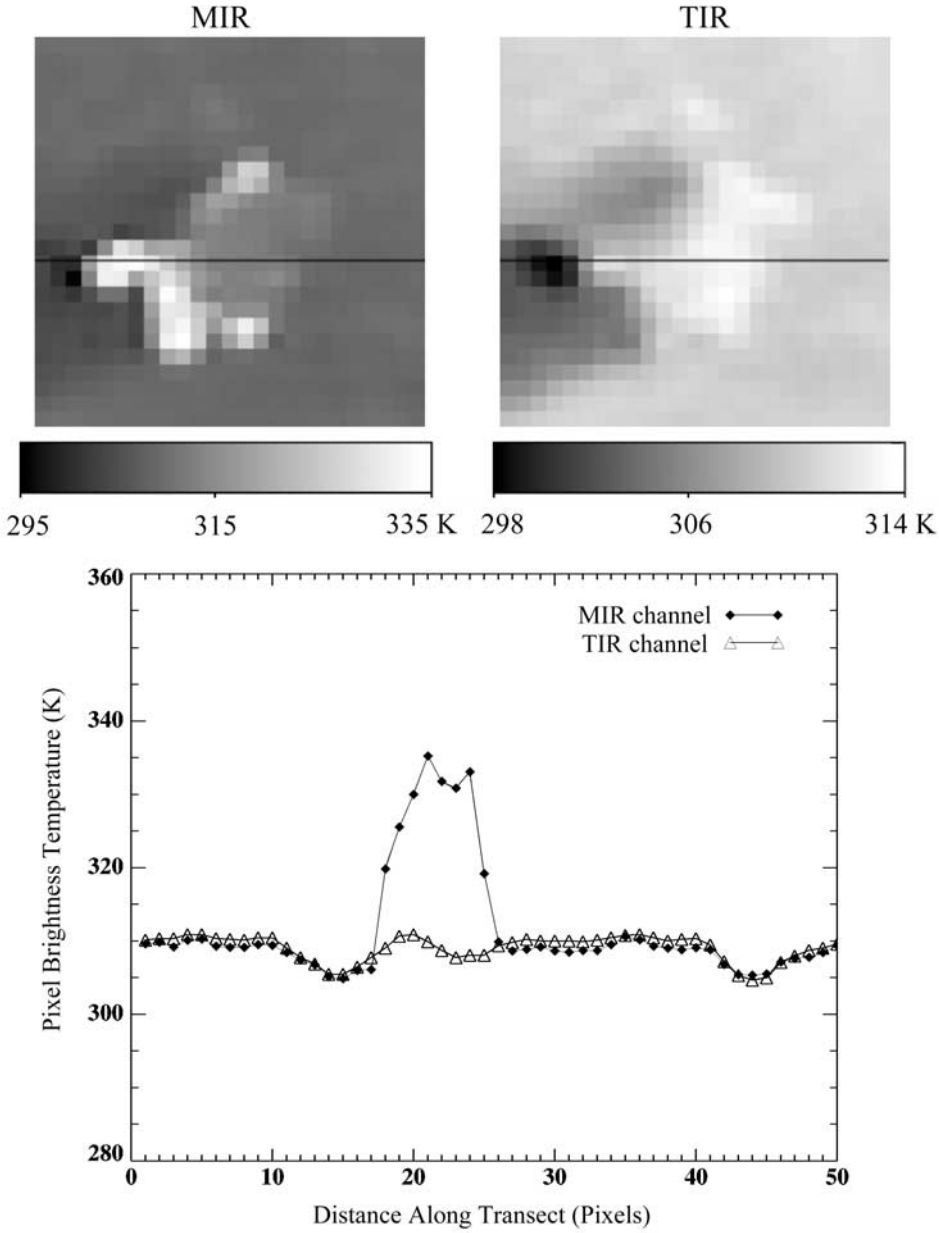

Figure 2. SEVIRI middle infrared and thermal infrared 25 × 25 pixel subsets of an active southern African savanna fire scene, along with the corresponding linear transect that highlights the fire pixels, greatly elevated MIR brightness temperatures when compared to those in the TIR.

ing certain thresholds to vary based on the image acquisition time, since, for example, nighttime images are typically more uniform in terms of ambient background temperature than are daytime images. In a similar way, the MODIS fire detection algorithm also incorporates different thresholds for daytime and nighttime imagery.

[14] Following *Giglio et al.* [2003a, 2003b], the SEVIRI fire detection algorithm works on statistics derived from the MIR, TIR, and MIR-TIR brightness temperature difference images. It first applies absolute thresholds to these images to detect ''potential'' fire pixels, which are then further assessed against a series of contextual tests whose thresholds are based on statistics derived from immediately neighboring nonfire ambient ''background'' pixels. The statistics are obtained from a background pixel window surrounding each potential fire pixel, the window starting off as a 3 × 3 matrix, being expanded by up to a factor of four in the x and y directions until 30% of its pixels are not themselves classed as potential fire pixels. Each potential fire pixel must pass all tests to be confirmed as a ''true'' fire pixel. The detection algorithm's parameters, shown in Table 1, were carefully optimized via a detailed visual analysis of a full set of diurnal SEVIRI images and resultant active fire maps.

[15] Figure 3 presents an example of SEVIRI fire detection. It is evident from the brightness temperature difference image (Figure 3c) that some fires remain undetected in the fire pixel mask (Figure 3d). These fires typically have FRP values too low to be detected with the current version of the algorithm, but could be detected by reducing some of the

Table 1. Absolute and Contextual Thresholds Applied in the Detection and Characterization of Active Fires With SEVIRI[a]

Function	Time of Day, UTC	Threshold
Detection of potential fire pixels	0600–0900	T4 > 293K, T11 > 285K, ΔT > 2.2K
Detection of potential fire pixels	0901–1500	T4 > 305K, T11 > 292K, ΔT > 3.5K
Detection of potential fire pixels	1501–0559	T4 > 285K, T11 > 280K, ΔT > 1.1K
Background characterisation	0600–0900	Valid pixels (BG) = T4 < 310K, ΔT < 6K
		Mean (BG4, BG11, BGΔT)
		Mdev (BG4, BG11, BGΔT)
Background characterization	0901–1500	Valid pixels (BG) = T4 < 322K, ΔT < 10K
		Mean (BG4, BG11, BGΔT)
		Mdev (BG4, BG11, BGΔT)
Background characterization	1501–0559	Valid pixels (BG) = T4 < 305K, ΔT < 5K
		Mean (BG4, BG11, BGΔT)
		Mdev (BG4, BG11, BGΔT)
Confirmation of true fire pixels	0600–0900	T4 > (Mean BG4 + 3.75 * Mdev BG4)
		ΔT411 > (Mean BGΔT + 3.9 * Mdev BGΔT)
		ΔT411 > (Mdev BG411 + 3K)
Confirmation of true fire pixels	0901–1500	T4 > (Mean BG4 + 3.5 * Mdev BG4)
		ΔT411 > (Mean BGΔT + 3.1 * Mdev BGΔT)
		ΔT411 > (Mdev BGΔT + 2.5K)
Confirmation of true fire pixels	1501–0559	T4 > (Mean BG4 + 2.3 * Mdev BG4)
		ΔT > (Mean BGΔT + 2.4 * Mdev BGΔT)
		ΔT > (Mdev BGΔT + 0.9K)

[a]Three sets of thresholds are used to account for illuminations variations over the 24-hour cycle. T4 = 3.9 μm brightness temperature, T11 = 10.8 μm brightness temperature, ΔT = 3.9–10.8 μm brightness temperature difference. BG = Background pixels (3.9 μm, 10.8 μm, 3.9–10.8 μm brightness temperature difference). Mdev = Standard deviation of the background pixel set, Mean = Mean of the background pixel set.

test thresholds. However, simple threshold reduction would result in an increased "false alarm" rate, and it is inevitable that a proportion of weakly emitting fires must remain undetected if such false alarms are to be kept to a minimum. It is, however, also true that further optimization of the SEVIRI fire detection algorithm may well be warranted once additional data are available to test its consistency over a full dry season. At present, comparisons to near simultaneously collected MODIS data indicate reasonable performance (Figures 3e and 3f).

4.2. Fire Characterization

[16] Fire characterization is carried out only on the set of confirmed SEVIRI "true" fire pixels detected using the algorithm described above. Fire characterization is a two-stage process. The first stage involves the derivation of per-pixel FRP using equation (3), with the background radiance $L_{bk,MIR}$ taken as the mean radiance ($\overline{L_{bk,MIR}}$) of the surrounding background pixel window. In reality, $\overline{L_{bk,MIR}}$ may differ somewhat from the true background radiance of the fire pixel, for example due to land cover differences or the impact of still-cooling postburn fire "scars" [*Wooster et al.*, 2003]. Any such difference introduces error to the FRP estimate, and the impact of this will be greatest when the fire proportion in a pixel is minimal [*Wooster et al.*, 2003; 2005]. Therefore the effect may be considered to be particularly important when analyzing data from low spatial resolution imaging systems such as SEVIRI, although it is also true that such systems will "average" the background temperature over larger areas and this may reduce the differences somewhat. In the FRP approach (equation (3)), the standard deviation ($\sigma L_{bk,MIR}$) of the background pixel radiances is used as a measure of the ambient background window's variability, and, following *Wooster et al.* [2003], is used to provide an indication of the potential uncertainty on FRP by providing a high and low FRP estimate using a

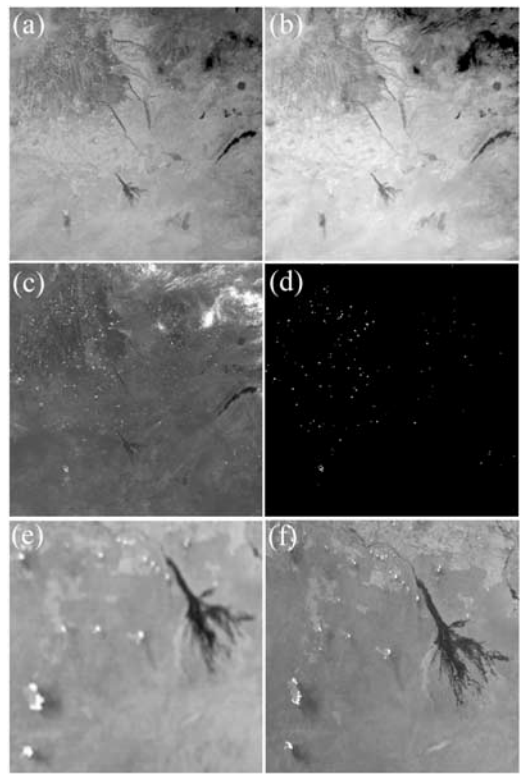

Figure 3. Imagery of southern Africa on 4 September 2003, showing numerous active fires. (a)–(d) Derived from SEVIRI imagery covering a 1200 km wide region, collected at 1212 UTC. (a) 3.9 μm, (b) 10.8 μm, (c) 3.9–10.8 μm brightness temperature difference, and (d) mask of confirmed active fire pixels. (e) and (f) SEVIRI and MODIS MIR image subsets centered on the Okavango delta region of Botswana and captured less than 15 min apart, where confirmed fire pixels are highlighted in white.

Table 2. Daytime and Nighttime Absolute and Contextual Thresholds Applied in the Detection and Characterization of Active Fires With MODIS[a]

Function	Temporal Conditions	Threshold
Potential fire detection	0900–1600	T4 > 320K, T11 > 285K, T411 > 15K
Potential fire detection	1601–0859	T4 > 290K, T11 > 285K, T411 > 10K
Background characterization	0900–1600	Valid pixels (BG) = T4 < 315K, T411 < 15K Mean (BG4, BG11, BGΔT) Mdev (BG4, BG11, BGΔT)
Background characterization	1601–0859	Valid pixels (BG) = T4 < 308K, ΔT < 10K Mean (BG4, BG11, BGΔT) Mdev (BG4, BG11, BGΔT)
Main fire detection	0900–1600	T4 > (Mean BG4 + 2.3 * Mdev BG4) T411 > (Mean BGΔT + 2.3 * Mdev BGΔT) T411 > (Mdev BGΔT + 6K)
Main fire detection	1601–0859	T4 > (Mean BG4 + 2.0 * Mdev BG4) T411 > (Mean BGΔT + 2.0 * Mdev BGΔT) T411 > (Mdev BGΔT + 4.5K)

[a]T4 = 3.9 μm brightness temperature. T11 = 11 μm brightness temperature. ΔT = 3.9 μm–11 μm brightness temperature difference. BG = Background pixels (3.9 μm, 11 μm, 3.9 μm–11 μm brightness temperature difference). Mdev = Mean standard deviation of the background pixels. Mean = Mean of the background pixels

low and high estimate of the ambient background radiance, respectively (i.e., using $L_{bk,MIR} = \overline{L_{bk,MIR}} \pm \sigma L_{bk,MIR}$ in equation (3)).

[17] The second stage of fire characterization involves clustering neighboring fire pixels into discrete groups via spatial adjacency criteria. Each pixel group is then considered to correspond to an individual fire, and the cumulative FRP of each fire calculated.

4.3. Accuracy Assessment With Respect to MODIS

[18] The fire detection and characterization capabilities of SEVIRI were assessed via comparison to near-simultaneous results derived from MODIS. MODIS currently represents the standard for operational global fire detection and characterization [*Giglio et al.*, 2003a, 2003b], including the derivation of FRP via two 3.9 μm channels having different gain settings and saturation temperatures (331 and 500 K respectively) [*Justice et al.*, 2002]. Limited comparisons between MODIS-derived FRP of individual fires and that derived simultaneously from higher spatial resolution imagery provided by the BIRD experimental "fire" satellite show good agreement, and where differences occur it is typically due to MODIS' inability to detect the low FRP fire pixels (<10 MW) that BIRD can reliably discriminate [*Wooster et al.*, 2003]. Such weakly emitting fires (FRP < 10 MW) are certainly not detectable by SEVIRI, and so MODIS represents a suitable validation data source for SEVIRI-derived FRP.

[19] Active fire FRP retrievals from five daytime MODIS (Terra and Aqua) level 1B (MOD021KM and MYD021KM) calibrated and geolocated radiance images collected over southern Africa were compared to those from SEVIRI. Cloud masks for each data set were again derived by applying an adjusted version of *Saunders and Kriebel*'s [1988] cloud-detection algorithm to the radiance images. For MODIS, this cloud mask was supplemented with that from the MOD14 product file corresponding to each MODIS level 1b radiance image. The fire mask contained within the MOD14 product was not used since, although performance of the version 4 algorithm is noted to be greatly improved over version 3 [*Giglio et al.*, 2003a, 2003b], it is a global product that could potentially be further refined for the specific late dry season southern African conditions encountered here. Instead, for consistency we applied the same fire detection methodology to MODIS as to SEVIRI, again adjusting the thresholds for optimal performance. In a similar way to the SEVIRI algorithm the MODIS algorithm used commences with an initial 3 × 3 pixel window centered over the candidate potential fire pixel to determine the contextual thresholds, expanding this up to 21 × 21 pixels or until over 30% of pixels surrounding the potential fire pixel are valid background pixels. Full algorithm details are given in Table 2.

4.3.1. Per-Fire FRP Comparison

[20] MODIS- and SEVIRI-derived FRP of matching fires were compared for fires with a MODIS view zenith angle $\leq 45^\circ$ (to avoid highly distorted, edge of swath MODIS views). Where a fire appeared to be double-counted by MODIS due to the so-called "bow-tie" effect (that results in ground areas, including fires, toward the edge of the swath being observed twice in successive scans) [*Wolfe et al.*, 2002] only one of the two MODIS fire clusters was considered. A total of 139 matched fires were selected, typically consisting of a larger number of clustered fire pixels in the MODIS data due to the higher spatial resolution. Figure 4 shows the results of this per-fire FRP comparison, with very strong agreement between the SEVIRI and MODIS data sets. SEVIRI underestimates FRP when compared to MODIS by an average of just 5%. The bias is low at −20 MW, although the degree of scatter is quite high at 213 MW, and 25% of the SEVIRI FRP observations differ from the coincident MODIS value by more than 40%. Three key factors are believed to contribute to this scatter: (1) the error related to the ambient background characterization; (2) the small but significant ($\leq$12 min) time difference between corresponding MODIS and SEVIRI observations, and (3) variation in retrieved FRP related to the subpixel location of the fire with respect to the sensor IFOV and point spread function. These effects introduce random rather than systematic error, and hence affect scatter and not bias. Since it is likely to be spatially or temporally integrated SEVIRI-derived FRP observations that are of most value, rather than instantaneous FRP of individual fires, the overall low bias of the SEVIRI FRP

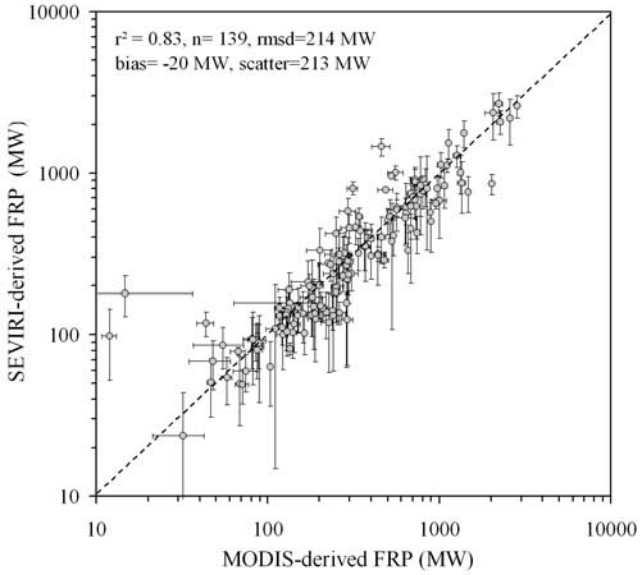

Figure 4. Comparison of FRP derived for the same fires viewed near simultaneously from SEVIRI and MODIS (r^2 = 0.83, n = 139, $p < 0.0001$), where a fire is defined as a contiguous cluster of active fire pixels. Fires from five near-coincident SEVIRI and MODIS scenes were used in the comparison, and error bars characterize the minimum and maximum FRP estimate obtained when ±1 standard deviation of the background window MIR radiance is added to $L_{bk,MIR}$ of equation (3). Error bars for a particular fire are generally higher for SEVIRI than for MODIS since the MIR signal of a particular fire pixel ($L_{h,MIR}$ in equation (3)) will generally be lower for the former sensor due to its larger pixel size. Thus a particular ambient background window variability will typically cause a larger perturbation to the FRP retrieval in the lower spatial resolution data.

with respect to MODIS suggests that the scatter may be relatively unimportant.

[21] A proportion of the noted bias between the SEVIRI- and MODIS-derived FRP maybe due to atmospheric influences, since the raw radiance data used were not adjusted for the absorbing and scattering effects of the atmosphere. This is because exact calculation of the atmospheric effect at each fire would require atmospheric humidity, temperature, and pressure profiles at that specific time and place. The atmospheric effect is likely to be quite similar for SEVIRI and MODIS however, since their MIR channels are both centered close to 3.9 μm, though perturbation of SEVIRI-derived FRP will be somewhat greater since its MIR channel has a significantly wider bandpass (SEVIRI: 3.63–4.21 μm; MODIS: 3.93–3.99 μm). The extent of the difference was assessed using radiative transfer modeling, carried out using MODTRAN 3.7 [*Berk et al.*, 1999] parameterized with 15 days of radiosonde atmospheric profile data collected at Maun Airport, Botswana during September 2003. Results indicate that for the same viewing zenith angle, atmospheric transmission in the SEVIRI MIR channel is 6% lower than in the MODIS MIR channel. This suggests that a large part of the mean 5% underestimate in SEVIRI FRP with respect to MODIS is likely to be due to wavelength dependent differences in atmospheric absorption. Mean MIR transmittance for the September data was calculated as 0.95 for MODIS (range 0.94 to 0.96) and 0.89 (range 0.77–0.94) for SEVIRI. A further contribution to the scatter comes from other unmodeled atmospheric effects, most notably the fact that the SEVIRI MIR channel bandpass encompasses both H_2O and CO_2 absorption features, gases that are present in increased concentration above fires. The narrowband MODIS MIR channel successfully avoids the major absorbing effects of these gases. As previously stated in section 2, though the smoke effects on the FRP signal have not been fully assessed, such perturbations are relatively minor in the MIR unless smoke is extremely thick, since the smoke particle diameter is smaller than the wavelength [*Kaufman et al.*, 1998a; *Wooster and Strub*, 2002].

4.3.2. Regional-Scale FRP Comparison

[22] For many emissions-related applications it is regional FRP/FRE estimates, rather than those of individual fires, that are important. To assess SEVIRI's ability to retrieve regional-scale FRP, results from 32 matching SEVIRI and MODIS Terra and Aqua (MOD021KM and MYD021KM) scenes were compared, these data being distributed over the full diurnal cycle (i.e., both daytime and nighttime) and taken over the 3–7 September 2003 period. All matching SEVIRI and MODIS scenes had time differences ≤12 min. Prior to the analysis, the MODIS data were subset to include only those pixels collected at view zenith angles ≤30° in order to prevent possible double-counting of fires and FRP due to the aforementioned MODIS "bow-tie" effect. The fire detection and characterization process summarized previously was applied to each MODIS subscene, and to the matching region of each contemporaneous SEVIRI image. The cumulative MODIS- and SEVIRI-derived subscene FRP (i.e., the FRP summed over all detected fire pixels) was then calculated. Figure 5 indicates the strong correlation between the regional FRP measure derived from the two sensors, although SEVIRI underestimates by, on average, 38% with respect to MODIS. Two factors are believed to contribute to this underestimation; (1) the reduced ability of SEVIRI to detect fire pixels <~100 MW, and (2) saturation of the SEVIRI MIR channel over the most strongly emitting fires. The latter is far less significant than the former since saturation is a relatively rare occurrence (see Figure 11 discussed later), while the MODIS data indicate that fires with FRP < 100 MW are rather frequent in certain areas of southern Africa. The few points where SEVIRI overestimates FRP with respect to MODIS are due to cases where large fires occurred under small clouds. In these situations a fire signature is still clearly apparent in the MIR channel data of each sensor (though typically reduced somewhat by the overlying colder cloud) but, while the small clouds were correctly identified by the MODIS cloud masking and the cloud-affected fires removed from the analysis, the SEVIRI cloud mask has failed to detect these small, sometimes subpixel, clouds and the FRP from these particular cloud-covered fires was included in the SEVIRI-derived regional FRP total.

4.3.3. Frequency-Magnitude Analysis

[23] Analyses of certain forest fire regimes suggests that perhaps as much as 99% of the total fire-affected area can be burned in the largest few percent of fires [*Strauss et al.*,

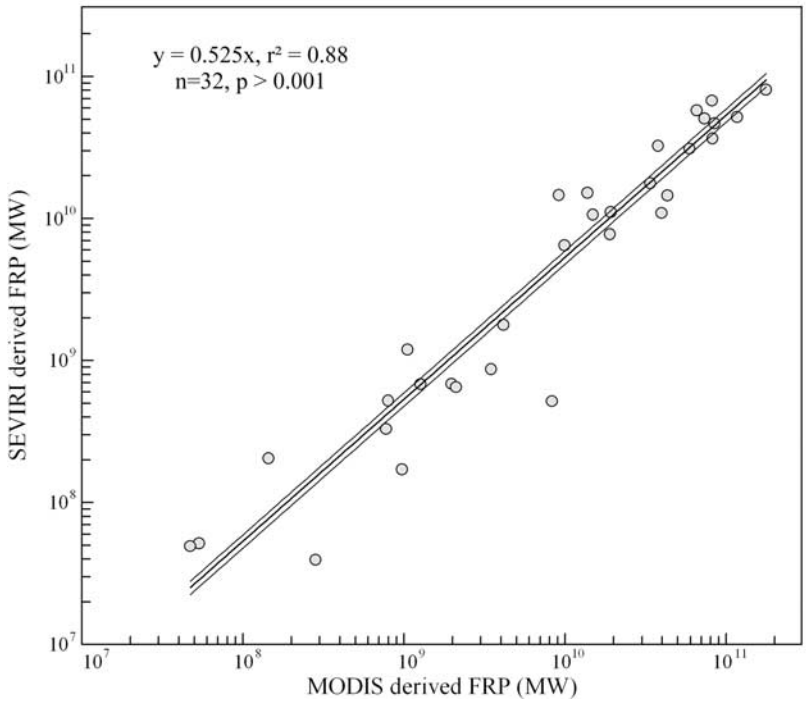

Figure 5. Comparison of cumulative FRP derived from 32 near-simultaneous SEVIRI and MODIS scenes covering 1900 × 2030 km regions of southern Africa. The least squares linear best fit through the origin and the 95% confidence limits for this relationship are also shown. The correspondence between the two data sets is statistically significant at the 0.01% level, although SEVIRI underestimates FRP by on average 38% (RMSD 56%) with respect to MODIS due to nondetection of weakly emitting fires having an FRP too low to be detected with the currently implemented SEVIRI fire pixel detection routine.

1989]. If this holds for FRP in the savanna, then the emissions' effect of small fires that go unobserved by SEVIRI may be relatively minor. However, the regional scale FRP comparisons between MODIS and SEVIRI (section 4.3.2) suggest that fire pixels <∼100 MW, which are observed by MODIS but may often be missed by SEVIRI, do contribute significantly to the overall regional-scale FRP. Further investigations were carried out using magnitude-frequency analysis of the SEVIRI FRP retrievals, again with comparison to simultaneous MODIS data. Magnitude-frequency assessments of burned area have been carried out by, for example, *Malamud et al.* [1998] and *Zhang et al.* [2003], while *Wooster and Zhang* [2004] recently used MODIS per-pixel FRP magnitude-frequency statistics to investigate boreal forest fire intensity distributions. The per-pixel FRP data from all 32 MODIS and SEVIRI scenes used in the regional-scale FRP comparison of section 4.3.2 were binned into 50 MW interval classes, and the magnitude-frequency relationships examined (Figure 6a). The FRP magnitude-frequency displays a predominantly inverse relationship on the log-log plot, agreeing with the findings of *Wooster and Zhang* [2004] for boreal environments. However, the SEVIRI data depart from this general trend at low FRP; and again this is the result of SEVIRI's reduced ability to detect the numerous fire pixels having FRP < ∼100 MW (see Figure 1). An assessment of the magnitude-frequency relationship of fire cluster size (i.e., the number of fire pixels within a fire) suggests a comparable relationship, with a similar frequency distribution but a different magnitude for the two sensors (Figure 6b). Again the reduced ability of SEVIRI to detect low FRP pixels is indicated by a lowering of the slope at the smallest cluster sizes (which typically have a lower per-pixel FRP).

[24] These SEVIRI and MODIS intercomparisons illustrate that while SEVIRI retrieves accurate, minimally biased estimates of FRP on a per-fire basis, any regional-scale FRP estimates derived from geostationary sensors such as SEVIRI should be treated as conservative. However, the SEVIRI-derived FRP data themselves may offer the potential to extrapolate the derived magnitude-frequency relationship to estimate the FRP provided by the more weakly burning, undetected fires. This is akin to methods used previously to estimate the amount of "unmapped" smaller burn scars in moderate and low spatial resolution EO-derived burned area products [*Zhang et al.*, 2003] and will be investigated further in section 7.

5. Fire Radiative Power Time Series

[25] SEVIRI's key advantage is the unprecedented temporal resolution it affords, allowing retrievals of FRP every 15 min over the entire African continent. The key advantage of MODIS is its ability to detect individual fires with low FRP. A comparison of the FRP time series provided by SEVIRI and MODIS over two fixed 5° × 5° areas of southern Africa (areas boxed in Figure 10) demonstrates the complementarities of these two data sources. SEVIRI

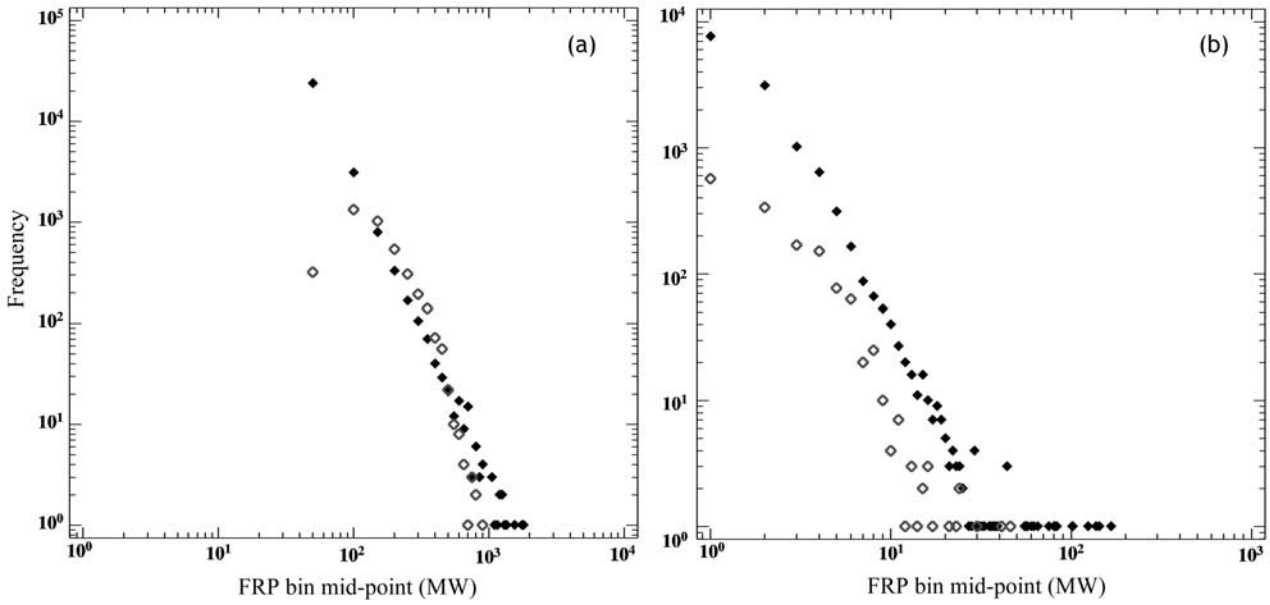

Figure 6. Magnitude-frequency statistics taken from the near coincident SEVIRI and MODIS scenes used for Figure 5, shown as the open and closed symbols, respectively. (a) Per-pixel FRP classed into 50 MW intervals, where for SEVIRI the relationship is seen to break down at FRP < ~100 MW due to the sensor's inability to detect these more weakly burning (i.e., smaller and/or less intense) fires. (b) Number of fire pixels comprising each individual fire, where the impact of the differing instrument spatial resolutions is illustrated by the higher frequency of fire clusters of a set size in the MODIS data when compared to SEVIRI. As cluster size decreases, the disparity between MODIS and SEVIRI increases since fires containing fewer pixels will generally have a greater proportion of low-FRP fire pixels, which are more likely to be detected by MODIS than by SEVIRI.

always observes each 5° × 5° area in full, but being a polar orbiting sensor MODIS sometimes observes only part of each. Therefore the Terra and Aqua MODIS scenes used in the comparison were limited to those covering greater than 70% of each 5° × 5° area (a total of 17 images). The SEVIRI and MODIS time series comparisons of each area are shown in Figure 7. To adjust for the effect of MODIS' varying observation area, the regional-scale MODIS FRP estimates are presented in both their "raw" form and in an "area weighted" form, adjusted for the proportion of the total 5° × 5° area observed during each MODIS overpass. A broadly similar pattern is evident from both SEVIRI and MODIS, indicating that for these regions and season MODIS is capable of characterizing the broad temporal trend of biomass burning. However, the diurnal fire dynamics are more clearly delineated by SEVIRI, though at the expense of FRP underestimation due primarily to the non-detection of low FRP fire pixels. This underestimation is most prevalent toward the diurnal peak of fire activity, most particularly on the days when there are particularly large numbers of low FRP fire pixels.

6. Validation of FRP and Biomass Combustion Relationships

[26] The relationship between remotely sensed FRP/FRE and the rates/totals of fuel mass combusted was first established using a series of experimental fires conducted in the UK with herbaceous and woody fuels (see the companion paper [*Wooster et al.*, 2005] and also *Wooster et al.* [2004] for details). In order to use SEVIRI-derived FRP to estimate biomass combustion rates and totals, it is necessary to confirm that these relationships are also applicable to southern African conditions. To assess this, experiments somewhat similar to those described by *Wooster et al.* [2002] and the companion paper [*Wooster et al.*, 2005] were conducted in Chobe National Park (CNP), northern Botswana (8.66°S, 24.5°E) around the time of SEVIRI image acquisition. The experiments were carried out in woodland savanna areas using a MIR (3.9 μm) thermal imaging camera positioned 5 m vertically above fires burning the available natural fuels (savanna grasses, grass and leaf litter, twigs and branches). CNP lies within an ecologically diverse region, transitioning between the arid/nutrient-rich savannas of the central Kalahari and the moist/nutrient-poor savannas of northern Zambia [*Huntley and Walker*, 1982; *Kamuhuza et al.*, 1997]. The grass species *Dactyloctenium giganteum*, *Eragrostis lehmanntana*, *Brachiaria nigropedota*, *Panicum maximum,* and *Aristida stipitala* characterized the study site, with grass height generally 0.75 m or less. Tree species supplying the majority of the leaf and woody litter were *Baikiaea plurijuga*, and the shrub/tree species *Combretum apiculatum*. Fuel moisture content was estimated to be 10–15% by oven drying samples at 70°C for 27 hours. Percentage (by weight) carbon contents of the individual fuel components in the region had been previously determined using a NCS2500 CHNS analyzer as 43.8 ± 2.6% (grass), 49.2 ± 1.3% (leaf), and 47.3 ± 1.3% (wood)

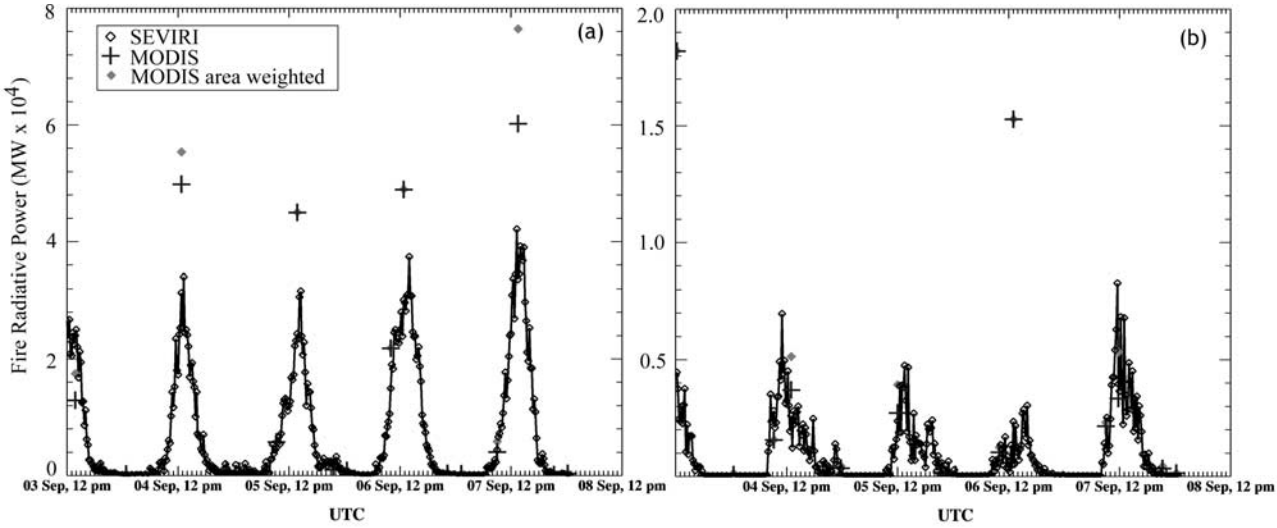

Figure 7. SEVIRI- and MODIS-derived FRP time series for two 5° × 5° areas in southern Africa, (a) 13–18°S, 17–22°W (SE Angola, NW Botswana), and (b) 10–15°S, 25–30°W (central Zambia). Areas are shown boxed in Figure 10. Since MODIS is a polar orbiting sensor (unlike the geostationary SEVIRI), it does not always image the complete 5° × 5° area on each overpass. Therefore the MODIS-derived FRP data are also presented weighted by the fraction of the 5° × 5° area observed (but in cases where the full 5° × 5° area is observed these points overlay). The data indicate the ability of SEVIRI to capture the diurnal dynamics of biomass burning, and it is evident that MODIS also provides a reasonable record of this. However, at the daily peak of biomass burning SEVIRI often underestimates FRP with respect to MODIS due to the presence of numerous weakly emitting fire pixels (cf. Figure 6). This is particularly the case for Figure 7b on 3 and 6 September 2003 when large numbers of weakly emitting fire pixels are detected by MODIS (280 and 470 pixels, respectively) but the majority are not detected by SEVIRI.

[*Smith et al.*, 2005]. Aboveground biomass estimates for the area varied between 0.1 and 0.4 kg/m^2, consistent with those reported in the literature for similar vegetation types and areas [*Scholes et al.*, 1996; *Hely et al.*, 2003; *Shea et al.*, 1996]. Three types of experimental fires were conducted. In the first, fuel was cut, collected, and burned on a sand-filled metal tray mounted on digitally logged scales. While this arrangement did not realistically represent the true geometry of a natural savanna grass sward, it did provide an accurate means of measuring the fuel mass actually combusted. The second set involved burning 1 m^2 fuel plots in situ, their being chosen on the basis of the plot appearing representative, in terms of biomass loading, when compared to the surrounding vegetation (whose biomass loading was assessed via destructive sampling of five 1 m^2 plots). This second set of fires represented essentially natural conditions (since the fuel was burnt in situ and without prior repositioning) but actual preburn fuel load was known only from sampling of the immediately surrounding vegetation. The third set represented an intermediate situation, where all fuel in a 1 m^2 plot was collected, weighed, and then repositioned and burned in situ. For all in situ fires, postfire char and ash were carefully collected, weighed, and subtracted from the prefire fuel load in order to calculate the fuel mass combusted.

[27] FRP was retrieved from the MIR camera imagery via application of equation (3), and FRE for each fire calculated via temporal integration of the individual FRP observations. To estimate biomass combusted, the linear relationship between FRE and fuel mass burned, derived for herbaceous and woody fuels during UK experiments by *Wooster et al.* [2005] was used. Figure 8 indicates that minimal bias is seen between the actual measured biomass combustion, and the FRE-derived estimate, indicating that the relationships derived in previous UK experiments are broadly appropriate for linking fire radiative power and energy and, respectively, fuel consumption rates and totals in the southern African dry season.

7. SEVIRI-Derived Biomass Burning Rates and Totals

[28] The SEVIRI-derived FRP time series of southern Africa were used with the validated linear relationship between FRP and biomass combustion rate to investigate the regional-scale combustion dynamics of southern Africa. As mentioned in section 4.3.2, fires do burn under cloud. Therefore it is likely that a certain proportion of cloud-covered pixels are obscuring active fires. To adjust for this, the cumulative FRP calculated for each SEVIRI image at a 0.5° × 0.5° and 1.0° × 1.0° grid cell resolution was weighted by the cloud fraction calculated at the same scale. This approach has been used previously to weight counts of active fire pixels made by the Tropical Rainfall Measuring Mission (TRMM) VIRS and NOAA AVHRR sensors [*Giglio et al.*, 2003a, 2003b; *Heald et al.*, 2003]. The inherent (but as yet unproven) assumption in all such approaches is that fires are, on average, equally likely to

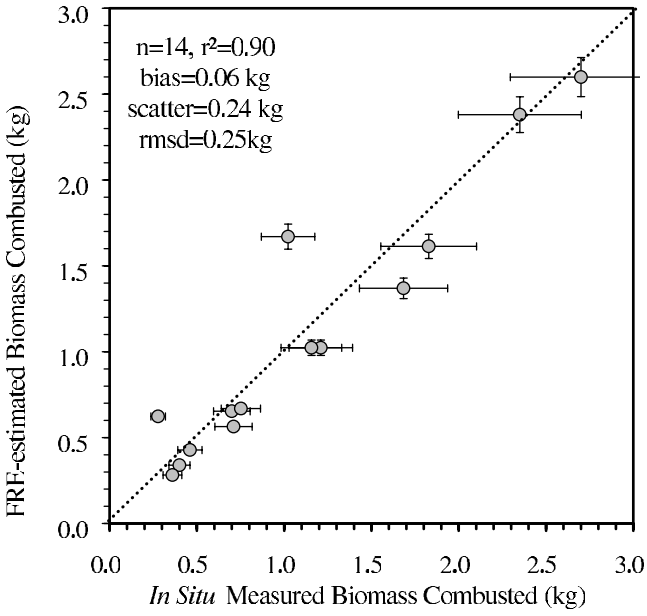

Figure 8. Comparison of fuel consumption measures, estimated for a series of small-scale experimental savanna fires conducted in Botswana in September 2003 (matching the timing of the SEVIRI and MODIS data used herein). The FRE-based fuel consumption estimate was derived using MIR camera-based measurements of fire radiative energy and the relationship between FRE and biomass combusted presented by *Wooster et al.* [2005], with error bars based on the 95% confidence level of the prediction of biomass combusted from FRE as estimated in that work. The in situ measure was derived via prefire and postfire sampling of fuel biomass, with error bars based on an assumed ±15% uncertainty in these measures. All values remain unadjusted for variations in fuel moisture content. The 1:1 line is shown for comparison.

occur beneath clouds as under clear skies. In any case, it seems unlikely that fires are more common under cloud than under clear skies, so the "observed" FRP and the "cloud adjusted" FRP effectively provide minimum and maximum FRP estimates for all fires whose FRP is of a magnitude detectable by SEVIRI.

[29] Strong diurnal variability in biomass burning is clearly apparent in FRP and biomass combustion rate over Angola (Figure 9a), Zambia (Figure 9b), and the whole of southern Africa (Figure 9c), with peak fire activity occurring between 1100 and 1400 UTC. This variability emphasizes the value of high temporal resolution data. Furthermore, it is apparent that in certain regions of southern Africa, the influence of cloud cover was relatively minor at this time. For example, in Angola "cloud adjusted" FRP is almost identical to observed FRP. Cloud cover increases toward the Equator, and in Zambia there is increased divergence between the observed and cloud-adjusted FRP measures.

[30] Active fires can be seen extending over the majority of the subcontinent, and the temporal development of the larger fires can be tracked over the full 4.5 days of the SEVIRI data set (Figure 10). As a minimum estimate, the observed FRP indicates that combustion rates over southern Africa reach at least 50 tons/s at the peak of biomass burning, an estimate that increases to a maximum of 74 tons/s when observed FRP is adjusted for cloud cover. Assuming that the magnitude of the atmospheric absorption effects, and the effects due to the nondetection of weakly emitting fire pixels, are broadly represented by the mean values determined in section 4.3, this peak combustion rate estimate increases further to ~135 tons/s.

[31] For southern African as a whole, integrating the observed FRP over the full 4.5-day duration provides an FRE total equating to 3.2 Tg of combusted biomass, and estimates for each individual country within the region are shown in Table 3. The southern Africa 3.2 Tg estimate increases to 4.3Tg and 5.1Tg when adjusted for cloud cover recorded at, respectively, the $0.5° \times 0.5°$ and $1.0° \times 1.0°$ grid cell resolutions (Figure 9c). Again, assuming the section 4.3 values for mean MIR atmospheric transmission and percentage FRP from undetected fires increases this estimate to ~7.9–9.3 Tg. On the basis of the fuel's percentage carbon contents, this represents a release of between 3.5 and 4.6 Tg of fuel carbon.

[32] Figure 11 confirms the generally low degree of saturation present in the SEVIRI data of active fires, which results in saturation effects having a small impact on the SEVIRI-derived regional FRP measures. As discussed previously, the sensors inability to detect low FRP fire pixels is a more significant effect, and some further indication of the extent of this maybe gained by extrapolating the observed FRP magnitude frequency relationship for all 67,422 fire pixels identified by SEVIRI, representing 23,422 individual fires (Figure 12). For fire pixels ≥100 MW the relationship is best fit by a reciprocal exponential model (which also represents the best fit relationship to the subset of SEVIRI and MODIS data shown in Figure 6a). On the basis of extrapolation of this power-law to estimate the frequency of the less intense fire pixels having FRP < 100 MW, the cumulative FRE of these latter hypothetical pixel set is estimated from the empirical best-fit as 2000 MJ, equivalent to 28% of the observed FRE from fire pixels ≥100 MW. However, as demonstrated in Figure 12, SEVIRI does actually observe a large number of fire pixels with FRP < 100 MW, it is just that their successful detection is less probable than that of fire pixels having a higher FRP, and a proportion of the actually existing fire pixels having FRP < 100 MW will therefore not have been detected (as indicated by the fact that the observed frequencies of FRP pixels <100 MW is lower than that predicted by the power law extrapolation). It is also likely that in a similar way to other active fire products, some proportion of the detected "fire" pixels having FRP < 100 MW will be false alarms, due for example to sunglint reflections from undetected small clouds. In the case of the 3–7 September observations studied here, the SEVIRI-detected fire pixels with FRP < 100 MW equate to a cumulative FRE of 1600 MJ, only 400 MJ less than the estimate derived from the power law extrapolation. Therefore the sum of modeled fires ≤100 MW and observed fires >100 MW increases total FRE (and thus the estimate of total fuel biomass combusted) by only 5% when compared to all observed fires (i.e., those fires detected by SEVIRI having FRP > 0). Of course this analysis is preliminary and very sensitive to the shape of the magnitude frequency distribution at low FRP, which may not be well

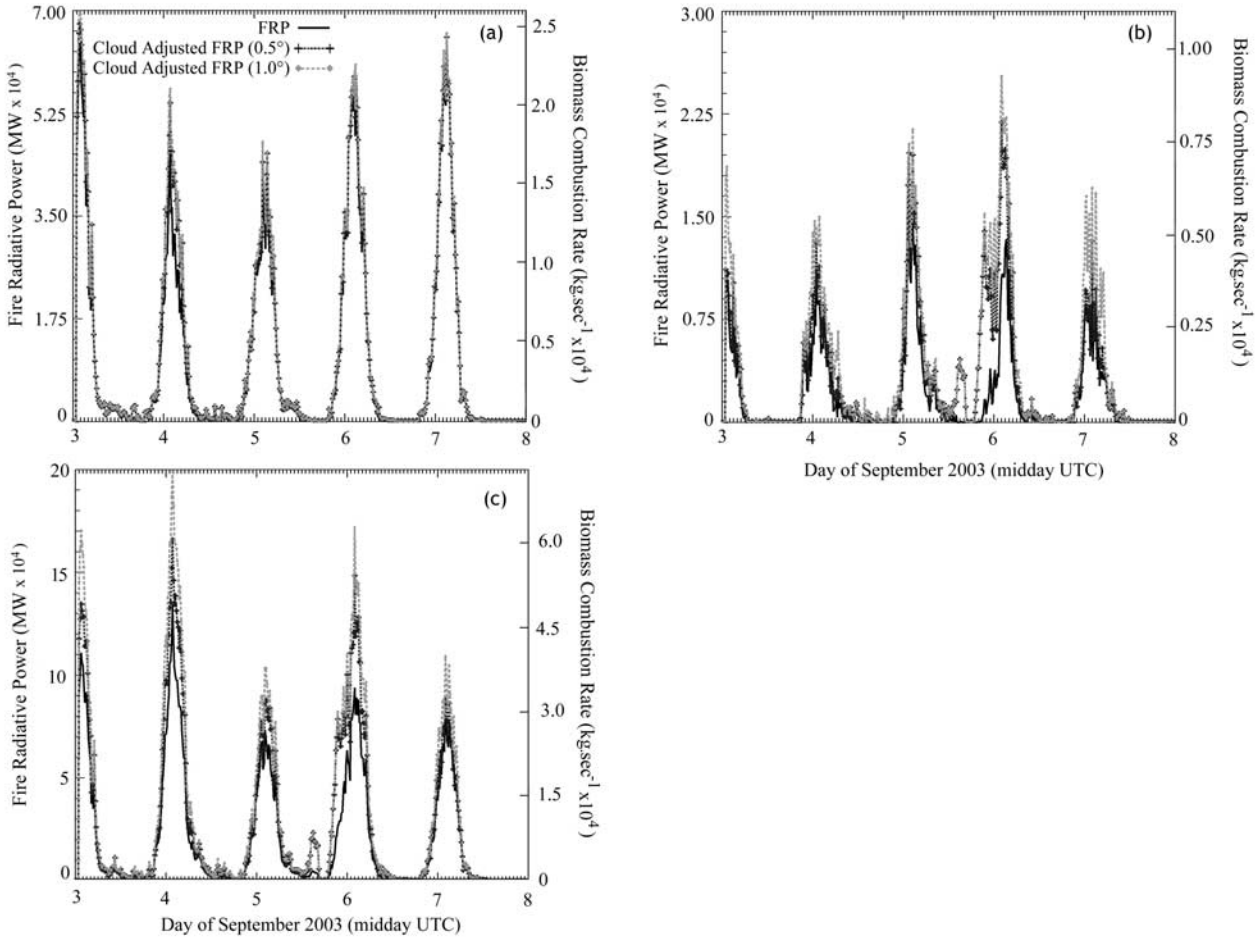

Figure 9. SEVIRI-derived FRP and biomass combustion rates for (a) Angola, (b) Zambia, and (c) southern Africa during 4.5 days in September 2003 (3–7 September). Ticks on the x-axis denote one hourly intervals, and the date labels are located at 1200 UCT each day. The timing of peak biomass burning is fairly stable, but large daily variations in fire activity magnitude are evident. Observed and "cloud-adjusted" FRP (i.e., observed FRP weighted by grid cell cloud fraction at 0.5° and 1.0° resolution) are both shown, and these generally show the same temporal trend. One exception is ~0100 UTC on 6 September in Figure 9b, where there is some fire activity on the western border of Zimbabwe, close to the border with Zambia. These regions have some cloud cover and this results in a small local peak in cloud-adjusted FRP in Figure 9b since the 0.5° and 1.0° grid cells include the Zimbabwe fires. Over the 4.5 days we estimate that a minimum of 1.68 Tg, 0.32 Tg, and 3.2 Tg of biomass was combusted in Angola, Zambia, and southern Africa, respectively, in order to produce the observed fire radiated energy. These are minimum estimates, and the actual biomass combustion will be higher due to nondetection of a certain proportion of the fire-radiated energy (see main text for details).

constrained by this relatively time-limited data set. In such circumstances, direct comparisons between SEVIRI and MODIS such as those of section 4.3, and ideally comparisons to even higher spatial resolution "FRP-capable" sensors such as BIRD [*Zhukov et al.*, 2005], may provide a better estimate of the extent of SEVIRI FRE underestimation than can magnitude-frequency analysis. All such studies would ideally need to be conducted using data taken throughout the full fire season since the fire size/intensity distribution will very likely vary over time.

8. Comparison With Other Data and Approaches

[33] Validation of fuel consumption measures produced over large regions is notoriously difficult. As outlined in the introduction, burned area has previously been the primary EO-derived product used in estimating wildfire fuel consumption, most particularly when combined with information on fuel load and combustion completeness (equation (1)). The range of per unit area fuel consumption possible in different land cover types is relatively well known. Therefore we divided our FRP-derived estimates of biomass combustion for individual fires by the corresponding burned area measure (mapped from MODIS) in order to assess the realism of the derived measures of per unit area fuel consumption. It should be noted that our measures represent values unadjusted for variations in fuel moisture content (measured at 10–15% in Botswana during fieldwork), whereas most burned area-based studies report the equivalent "dry weight" values.

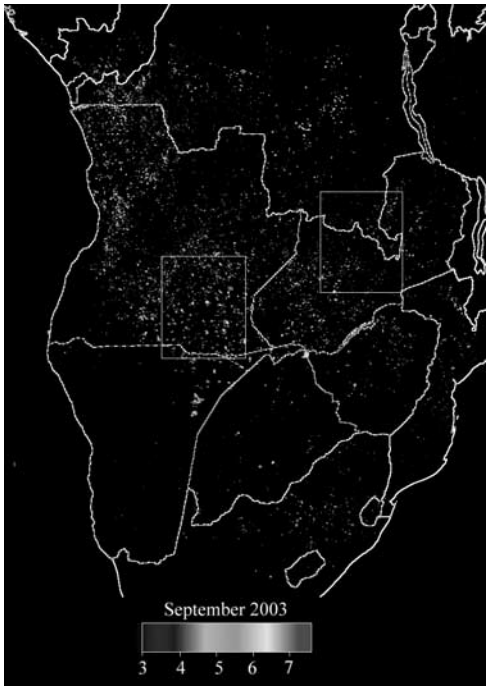

Figure 10. SEVIRI derived spatial distribution and timing of active fires in southern Africa from 1200 UTC on 3 September until 2357 UTC on 7 September 2003. Boxes indicate the $5^\circ \times 5^\circ$ regions whose FRP temporal trends are plotted in Figure 7. See color version of this figure at back of this issue.

[34] Burnt area was mapped via comparison of prefire and postfire MODIS scenes, collected on 28 August and 6 September 2003, respectively. Although a range of techniques exist for automated burned area mapping [e.g., *Eva and Lambin*, 1998; *Fraser et al.*, 2000; *Stroppianna et al.*, 2003], many of these use SWIR bands in addition to those in the NIR or visible spectral regions, and since the MODIS SWIR bands are imaged at 500 m spatial resolution their use would decrease the spatial precision of mapping below that which can be obtained with the MODIS 250 m spatial resolution red and NIR spectral channels. Since we were working with a very limited area and time period, it was more appropriate to use the 250 m resolution data to preserve the highest spatial detail. The response of the MODIS red channel to burning is somewhat dependent on land cover type and atmospheric state, potentially reducing the contrast between burned and unburned surfaces and affecting the ability to use this spectral channel for the discrimination. However, the NIR channel is well suited to identification of burned areas and less sensitive to atmospheric scattering, and *Roy et al.* [2002] and *Smith et al.* [2002] have previously shown this waveband to be the most appropriate single wavelength for mapping burnt areas in African savannas. In particular, NIR reflectance strongly decreases on burning, due to the loss of vegetation and its replacement with low albedo ash [*Zhang et al.*, 2003; *Silva et al.*, 2004]. Careful manual interpretation allowed us to highlight ground areas where significant land cover change occurred between the two MODIS images, the vast majority of this being due to wildfire events. Only areas where active fires were identified by SEVIRI, and the corresponding burnt area identified by MODIS, were selected for inclusion, and we are confident that in all selected areas the NIR reflectance change was due to fire. To be additionally certain, only those areas where SEVIRI detected no active fires prior to the date of the first MODIS image, and where fires ceased prior to the last MODIS image, were incorporated in the analysis.

[35] Using this method, we selected matching FRP and burned area data for 46 fires distributed throughout southern Africa. Burnt area, observed FRE, and total biomass combusted ranged from 3.8 to 201 km^2, 0.20 to 109 TJ, and 75 to 40,000 tons, respectively. From these data we estimated per unit area fuel consumption for each fire, categorized by land cover type taken from the Global Landcover 2000 categorization [*Mayaux et al.*, 2004]. With the exception of open shrubland, the calculated per unit area fuel consumption generally decreases with decreasing woody cover (Table 4). This is expected as dead leaves and woody litter from the canopy contribute additional dry biomass to the otherwise primarily herbaceous fuel load. While the totals listed in Table 4 appear quite low, it should be remembered that the estimates based on observed FRE are uncorrected for potential atmospheric effects and are subject to the reduced-detection of pixels whose FRP is $<\sim$100 MW. Furthermore, the estimates based on both the observed and adjusted FRE measures both assume that all areas within the MODIS-derived "burn scar" are 100% burned, whereas, in reality, subpixel patchiness does exist, particularly at the "burn scar" edge pixels. Because of this patchiness, MODIS will typically overestimate the size of burned savanna areas when compared to higher spatial resolution sensors such as Landsat ETM+, perhaps by around 10–20% (A. M. Smith et al., Assessment of EO-derived burned area measures in southern African savannas, manuscript in preparation, 2005), though of course in terms of total regional burned area this maybe counteracted by MODIS' failure to detect burned areas very significantly smaller than those considered here. *Ward et al.* [1996] and *Scholes et al.* [1996] provide in situ measured data with

Table 3. Country-Scale Estimates of Minimum Wildfire Fuel Combustion for the 4.5 Days of Data Represented by Figure 10 (1200 UTC on 3 September 2003 until 2357 UTC on 7 September 2003), Derived Using Observed Retrievals of Fire Radiative Power Made by the SEVIRI Radiometer[a]

Country	Biomass Combusted, Tg
Angola	1.68
Botswana	0.09
Malawi	0.05
Namibia	0.59
South Africa	0.24
Zambia	0.32
Zimbabwe	0.17

[a]Actual biomass combustion will be higher than this minimum due to nondetection of a certain proportion of the fire-emitted energy due to cloud cover, atmospheric absorption of the upwelling fire-emitted energy, and the non-detection of small and/or weakly burning fires (see text for details). Taking these effects for southern Africa as a whole, a first estimate of these effects suggests biomass consumption maybe perhaps $\sim$3X the minimum estimates shown here.

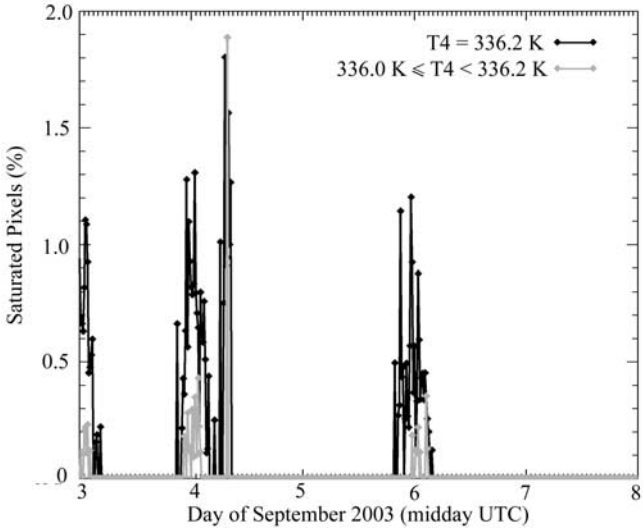

Figure 11. SEVIRI fire pixel saturation over southern Africa for 3–7 September 2003. SEVIRI was designed to saturate at a MIR brightness temperature (T4) in excess of 335 K [*Schmetz et al.*, 2002] and in fact a maximum T4 of 336.2 K is recorded in the level 1.5 data. Even at its peak on 4 September, less than 2% of the detected fire pixels reached this MIR brightness temperature, and less than 4% had T4 $\geq$ 336 K. On other days, less than half this percentage lies in the 336–336.2 K range, and no saturated pixels are present on 5 or 7 September. In the total data set covering 3–7 September, only 0.45% of the detected fire pixels have the maximum 336.2 K MIR brightness temperature, while a total of 2.2% are within 1.2 K of the saturation limit (i.e., have T4 in the range 335–336.2 K).

which to compare the FRE-derived fuel consumption estimates. For Kruger National Park, South Africa, and central/southern Zambia, *Ward et al.* [1996] measured fuel consumptions of 0.16–0.59 and 0.21–0.52 kg/m^2, respectively, including both grassland and woodland. *Scholes et al.* [1996] provide details of measured mean fuel loads in African fire-prone vegetation (grasslands, savannas, woodlands, forests) from a variety of past studies, indicating a range of 0.15–0.55 kg/m^2. Therefore the range of FRE-derived per unit area fuel consumption measures reported in Table 4 are in fact broadly similar to these in situ measures, and further comparisons based on this approach will be conducted once contemporaneous dry season data are available from SEVIRI and MODIS throughout the entire dry season.

[36] We can further compare the general magnitude of our for southern Africa biomass combustion totals with those from previous studies if we assume that the 4.5-day period studied here is broadly representative of fire activity throughout the 6 month local dry season (though there is some evidence that fire activity is likely to be of greater magnitude between the months of July and September) [*Dwyer et al.*, 2000; *Swap et al.*, 2003]. This assumption leads to a SEVIRI-derived estimate based on observed FRE of 130 Tg for southern Africa, rising to 200–235 Tg including the correction for cloud cover and atmospheric absorption, and ~320–380 Tg including adjustment for the nondetection of weakly emitting fire pixels (based on the earlier comparison of MODIS and SEVIRI regional FRP). An early estimate by *Hao et al.* [1996] concluded that around 1200 Tg of biomass are combusted annually in southern Africa, while *Scholes et al.* [1996] derived widely ranging estimates of 90–264 Tg using a modeling approach and 247–2719 Tg using a land cover classification based approach. Most recently, *Korontzi et al.* [2004] used burned area data for a shorter 1 month period, along with information on fuel load and combustion completeness variations with land cover, to provide an estimate of 79 Tg of biomass combustion for southern Africa wildfires in September 2000, though substitution of an alternative burned area product decreased this to 18 Tg. It seems likely that problems in estimating fuel load and combustion efficiency introduce uncertainties of perhaps comparable magnitudes to that introduced by burned area, but since the estimate is for the same month as our SEVIRI-based work a comparison to our results is warranted (though *Korontzi et al.* [2004] study September 2000 rather than 2003). Extrapolating our 4.5 day FRE-derived estimates to the entire month of September provides biomass combustion estimates of 20 Tg (based on observed FRP) to 65 Tg (FRP adjusted for the potential effects of cloud cover, atmospheric absorption, and the nondetection of low FRP fire pixels), which is rather similar to the range provided by *Korontzi et al.* [2004] and well below the maximum values obtained in

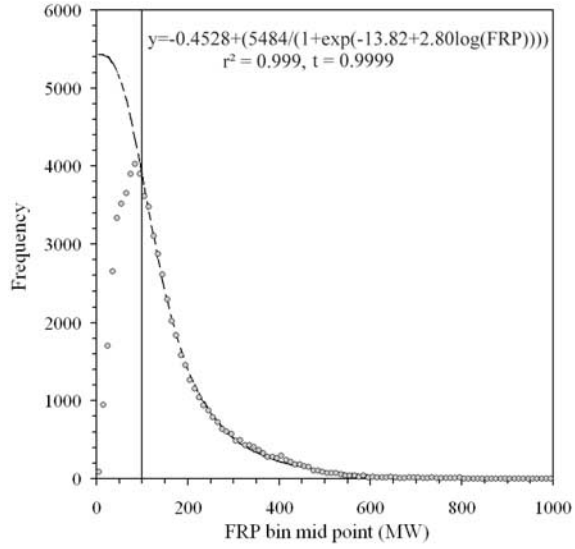

Figure 12. Magnitude-frequency of fire pixel FRP derived from 432 SEVIRI scenes of southern Africa, i.e., data used in Figure 9c and Figure 10, binned into 10 MW intervals. Vertical line indicates the 100 MW FRP threshold below which fire pixel frequency is increasingly underestimated due to a combination of sensor spatial resolution and fire detection algorithm sensitivity resulting in active fire pixel nondetections. For FRP $\geq$ 100 MW the FRP frequency-magnitude relationship is well fit by a reciprocal exponential model (dotted line) whose equation and coefficient of determination (r^2) are shown. The model can be extrapolated to estimate the true frequency of low FRP fire pixels <100 MW.

Table 4. Estimated Per Unit Area Fuel Consumption in Key Fire-Affected Land Cover Classes of the Global Land Cover 2000 Categorization [*Mayaux et al.*, 2004][a]

Land Cover Class	Tree Layer, %	Shrub Layer, %	Grass Layer, %	Sample Number	Per Unit Area Fuel Consumption Using Observed FRE, kg/m^2	Per Unit Area Fuel Consumption Using Adjusted FRE, kg/m^2
Forest	>40	-	-	5	0.27 ± 0.08	0.49 ± 0.15
Woodland	15–40	>15	<15	12	0.15 ± 0.11	0.27 ± 0.20
Shrubland	<15	>15	>40	10	0.05 ± 0.03	0.09 ± 0.05
Open Shrubland	<5	>15	>40	10	0.08 ± 0.05	0.15 ± 0.09
Croplands	-	-	>50 (crops)	9	0.06 ± 0.04	0.10 ± 0.07

[a]The original classification incorporates 27 land cover classes, here amalgamated into five broader categories whose percentage cover of tree, shrub, and grasses are shown. Per unit area fuel consumption was estimated using SEVIRI-derived fire radiative energy retrievals and MODIS-derived burnt area estimates for 46 fires distributed over the land cover classes listed. Two fuel combustion estimates are listed for each class, corresponding to that calculated using only the observed FRE, and that using the observed FRE adjusted for the mean calculated MIR atmospheric absorption and the mean FRE underestimation caused by SEVIRI's inability to detect the lowest FRP fire pixels (as evaluated via comparison to MODIS; see Figure 5). Cloud cover effects were not adjusted for since, as far as was possible, cloud-free areas were chosen for the analysis. In each land cover class between five and 12 fires were sampled, and the mean fuel consumption ±1 standard deviation is shown.

the above-cited studies (assuming September is not an unusually low combustion month). Thus our FRE-derived estimate broadly agrees with the fuel range of consumption deduced from the most recent application of equation (1) in the same region and time of year.

[37] Clearly, much further work is required, not least in determining the optimum methods for adjusting the SEVIRI FRP observations for the already mentioned effects that depress the time-integrated FRE below the true value of fire-emitted energy. At present, the SEVIRI-derived FRE observations appear to represent excellent estimates of the minimum amount of fire-emitted energy, and once fully tested and validated methods of adjusting the observations for the effects of cloud cover, atmospheric absorption, and the nondetection of low FRP fire pixels become available they should also provide a solid estimate of the upper bound on this parameter. We feel confident that the physical basis of the FRE method makes it a strong candidate for the new, independent emissions estimation route called for by *Andrae and Merlet* [2001], and that the approach can be used to supplement, and perhaps in some cases supersede, exiting methods based on remote sensing of burned area and assumed or modeled fuel loads and combustion completeness parameters.

[38] With regard to the temporal trajectory of the number of active fire pixels and active fires over southern Africa, this follows a similar trend to that of FRP (Figure 13a) and is consistent with the active fire temporal dynamics for southern Africa derived from TRMM VIRS by *Giglio et al.* [2003a, 2003b], and that derived from geostationary surveillance satellites originally designed for missile early warning [*Pack et al.*, 2000]. The maximum number of fire pixels observed within a single SEVIRI southern African scene varies daily between ~350 and 900, while the peak number of fire clusters is less variable at between 180 and 300. Typical ratios of total scene FRP to total number of fire pixels are between ~50 and 200 MW/pixel, with a strong diurnal cycle (Figure 13b). Fire pixel numbers have been used to within studies of emissions inventory and atmospheric transport [e.g., *Generoso et al.*, 2003; *Reid et al.*, 2004; *Schultz*, 2002] but the temporally variable value of mean FRP per pixel found here suggests that using fire counts alone (without consideration of their varying intensity) may introduce substantial error. If such fire count data are to be used, then it seems important that they are taken at the same time each day since both the total number of fire pixels, and the mean FRP/fire pixel count, display a strong diurnal trend (Figure 13).

9. Conclusions

[39] This study has demonstrated for the first time the retrieval of biomass burning rates from geostationary remote sensing observations of fire radiative power (FRP). The full diurnal cycle of FRP is presented for areas of southern African at the regional, country, and semicontinental scale, based on observations made by the Meteosat-8 SEVIRI radiometer. For the first time, remotely derived fuel combustion rates are presented on a subhourly time step most suitable for linking to mesometeorological models of emissions transport. The high temporal resolution afforded by the geostationary imager provides the platform from which to derive the total emitted fire radiative energy and the total fuel consumption via the temporal integration of FRP. The data highlight the strong diurnal variability in African biomass burning and indicate that over a 4.5 day period an absolute minimum of 3.2 Tg of biomass was burnt in southern Africa, rising to perhaps 9.3 Tg when the observed FRE is adjusted for effects that cause its inherent underestimation.

[40] On the basis of the work presented and that of the related papers cited herein, the FRP approach appears to offer an attractive means for estimating wildfire fuel consumption, not least because it is based on a physically observable variable (i.e., fire-emitted radiative power) directly related to the biomass combustion rate. The method removes many of the parameterization difficulties involved existing approaches based on the *Seiler and Crutzen* [1980] algorithm and remote sensing measurements of burned area, seemingly avoiding major dependence on fuel type, biomass loading or combustion completeness parameters which have been highlighted by *French et al.* [2004] and others as major barriers to reducing uncertainly in combustion estimates. Furthermore, when calculated at a sufficiently

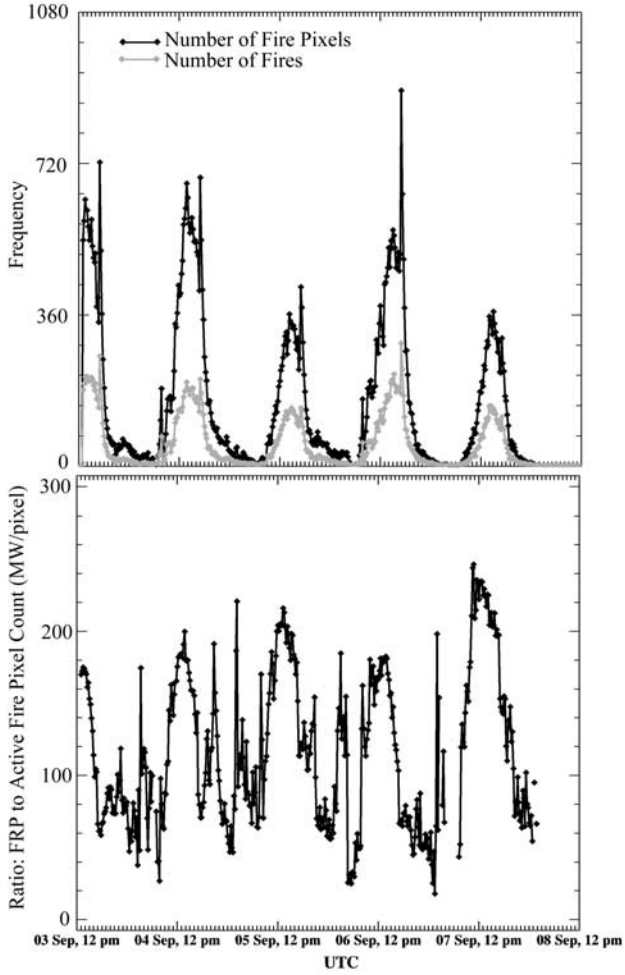

Figure 13. (a) Temporal profile of active fire counts and active fire clusters over southern Africa illustrating the dynamic nature of fire activity. (b) The mean FRP per active fire pixel displays considerable variability, some of which appears related to the timing with respect to the fire diurnal cycle.

high temporal resolution, the FRP approach provides previously unavailable information on diurnal variation in combustion rates and locations that, potentially, can be used to improve links between emissions sources and models of pollutant transport within the lower atmosphere.

[41] We have compared FRP magnitudes derived via SEVIRI to near-simultaneous FRP retrievals made using the same principles from polar-orbiting EOS-MODIS data. Provided the fire is large and/or intense enough to be detected by both imagers, comparisons of per-fire FRP show good agreement. However, though SEVIRI offers the distinct advantage over MODIS of an almost two-order of magnitude higher temporal resolution, the regional-scale SEVIRI FRP retrievals are limited by a reduced ability to detect fire pixels whose FRP $< \sim$100 MW, compared to MODIS that can confidently detect fire pixels down to $\sim$10 MW. The lowest intensity fires are therefore missed by SEVIRI and so in some circumstances the combined use of both SEVIRI and MODIS FRP retrievals will certainly be advantageous. Furthermore, both sensors fail to detect fires burning under thick meteorological cloud and, though cloud cover is often relatively sparse during the peak periods of fire activity, it seems likely that a synergistic approach, using active-fire observations of FRP and postfire observations of burned area, may provide the most accurate means to estimate overall fuel consumption. Ongoing research is considering how best to combine MODIS and SEVIRI data to meet this requirement, and also to better quantify the potential measurement limitations to FRP retrieval, such as the effect of viewing through thick smoke or tree canopies.

[42] **Acknowledgments.** This study was supported by NERC New Observing Techniques (NOT) grant NER/Z/S/2001/01027. SEVIRI data were kindly provided under an ESA/EUMETSAT AO, while MODIS data were obtained via the NASA Goddard Space Flight Center (GSFC) and EROS Data Centre DAACs. The authors would like to thank the Government of Botswana and in particular the Department of Wildlife and National Parks for their support and assistance in conducting the field component of this research and EUMETSAT for their unswerving support and excellent supply of data. We would also like to thank the reviewers for their very positive and helpful comments on this manuscript.

References

Aminou, D. M. A., B. Jacquet, and F. Pasternak (1997), Characteristics of the Meteosat second generation radiometer/imager: SEVIRI, in *Proceedings of SPIE Europto Series*, vol. 3221, pp. 19–31, SPIE, Bellingham, Wash.

Andreae, M. O. (1991), Biomass burning: Its history, use and distribution and its impact on the environmental quality and global climate, in *Global Biomass Burning: Atmospheric, Climatic and Biospheric Implications*, edited by J. S. Levine, pp 2–21, MIT Press, Cambridge, Mass.

Andreae, M. O., and P. Merlet (2001), Emission of trace gases and aerosols from biomass burning, *Global Biogeochem. Cycles*, *15*, 966–995.

Arino, O., J.-M. Melinotte, and G. Calabresi (1993), Fire, cloud, land, water: The Ionia AVHRR, *Rep. E0Q 41*, Eur. Space Agency, Noordwijk, Netherlands.

Berk, A., et al. (1999), MODTRAN4 radiative transfer modeling for atmospheric correction, *Proceedings SPIE Optical Spectroscopic Techniques and Instrumentation for Atmospheric and Space Research III*, 3756.

Boles, S. H., and D. L. Verbyla (1999), Effect of scan angle on AVHRR fire detection accuracy in interior Alaska, *Int. J. Remote Sens.*, *20*, 3437–3443.

Dozier, J. (1981), A method for satellite identification of surface temperature fields of sub-pixel resolution, *Remote Sens. Environ.*, *11*, 221–229.

Dwyer, E., S. Pinnock, J.-M. Gregoire, and J. M. C. Pereira (2000), Global spatial and temporal distribution of vegetation fires as determined from satellite observations, *Int. J. Remote Sens.*, *21*, 1289–1302.

Eva, H., and E. F. Lambin (1998), Burnt area mapping in Central Africa using ATSR data, *Int. J. Remote Sens.*, *19*, 3473–3497.

Fazakas, Z., M. Nilsson, and H. Olsson (1999), Regional forest biomass and wood volume estimation using satellite data and ancillary data, *Agric. For. Meteorol.*, *98–99*, 417–425.

Fraser, R. H., Z. Li, and J. Cihlar (2000), Hotspot and NDVI differencing synergy (HANDS): A new technique for burned area mapping over Boreal forest, *Remote Sens. Environ.*, *74*, 362–376.

French, N. H., P. Goovaerts, and E. S. Kasischke (2004), Uncertainty in estimating carbon emissions from boreal forest fires, *J. Geophys. Res.*, *109*, D14S08, doi:10.1029/2003JD003635.

Fuller, D. O., S. D. Prince, and W. L. Astle (1997), The influence of canopy strata on remotely sensed observations of savanna-woodlands, *Int. J. Remote Sens.*, *18*, 2985–3009.

Generoso, S., F.-M. Breon, O. Boucher, and M. Schultz (2003), Improving the seasonal cycle and interannual variations of biomass burning aerosol sources, *Atmos. Chem. Phys. Disc.*, *3*, 1973–1989.

Giglio, L., and C. O. Justice (2003), Effect of wavelength selection on characterisation of fire size and temperature, *Int. J. Remote Sens.*, *24*, 3515–3520.

Giglio, L., and J. D. Kendall (2001), Application of the Dozier retrieval to wildfire characterisation: A sensitivity analysis, *Remote Sens. Environ.*, *77*, 34–49.

Giglio, L., J. D. Kendall, and C. O. Justice (1999), Evaluation of the global fire detection algorithms using simulated AVHRR infrared data, *Int. J. Remote Sens.*, *20*, 1947–1985.

Giglio, L., J. D. Kendall, and R. Mack (2003a), A multi-year active fire data set for the tropics derived from TRMM VIRS, *Int. J. Remote Sens.*, *24*, 4505–4525.

Giglio, L., J. Descloitres, C. O. Justice, and Y. J. Kaufman (2003b), An enhanced contextural fire detection algorithm for MODIS, *Remote Sens. Environ.*, *87*, 273–282.

Govaerts, Y. M., J. M. Pereira, B. Pinty, and B. Mota (2002), Impact of fires on surface albedo dynamics over the African continent, *J. Geophys. Res.*, *107*(D22), 4629, doi:10.1029/2002JD002388.

Hao, W. M., D. E. Ward, G. Olbu, and S. P. Baker (1996), Emissions of CO^2, CO and hydrocarbons from fires in diverse African savanna ecosystems, *J. Geophys. Res.*, *101*, 23,577–23,584.

Heald, C., D. Jacob, P. Palmer, M. Evans, G. Sachse, H. Singh, and D. Blake (2003), Biomass burning emission inventory with daily resolution:Application to aircraft observations of Asian outflow, *J. Geophys. Res.*, *108*(D21), 8811, doi:10.1029/2002JD003082.

Hely, C., S. Alleaume, R. J. Swap, H. H. Shugart, and C. O. Justice (2003), SAFARI-2000 characterisation of fuels, fire behavior, combustion completeness, and emissions from experimental burns in infertile grass savannas in western Zambia, *J. Arid Environ.*, *54*, 381–394.

Huntley, B. J., and B. H. Walker (1982), *Ecology of Tropical Savannas*, *Ecol. Stud.*, vol. 42, Springer, New York.

Ichoku, C., Y. J. Kaufman, L. Giglio, Z. Li, R. H. Fraser, J.-Z. Jin, and W. M. Park (2003), Comparative analysis of daytime fire detection algorithms using AVHRR data for the 1995 fire season in Canada: Perspective for MODIS, *Int. J. Remote Sens.*, *24*, 1669–1690.

Intergovernmental Panel on Climate Change (IPCC) (2001), *Climate Change 2001: The Scientific Basis*, edited by J. T. Houghton et al., Cambridge Univ. Press, New York.

Justice, C. O., L. Giglio, S. Korontzi, J. Owens, J. T. Morisette, D. Roy, J. Descloitres, S. Alleaume, F. Petitcolin, and Y. Kaufman (2002), The MODIS fire products, *Remote Sens. Environ.*, *83*, 244–262.

Kamuhuza, A., G. Davis, S. Ringrose, J. Gambiza, and E. Chileshe (1997), The Kalahari Transect: Research on global change and sustainable development in Southern Africa, *Rep. 42*, Int. Geosphere-Biosphere Progr., Stockholm.

Kaufman, Y. J., and C. O. Justice (1998), MODIS fire products, in *Algorithm Theoretical Basis Document*, *Version 2.2, Rep. EOS-ID 2741*, MODIS Fire Team, NASA Goddard Space Flight Cent., Greenbelt, Md.

Kaufman, Y. J., L. Remer, R. Ottmar, D. Ward, R.-L. Rong, R. Kleidman, R. Frase, L. Flynn, D. McDougal, and G. Shelton (1996), Relationship between remotely sensed fire intensity and rate of emission of smoke: SCAR-C experiment, in *Global Biomass Burning*, edited by J. Levine, pp. 685–696, MIT Press, Cambridge, Mass.

Kaufman, Y. J., R. G. Kleidman, and M. D. King (1998a), SCAR-B fires in the tropics: Properties and remote sensing from EOS-MODIS, *J. Geophys. Res.*, *103*, 31,955–31,968.

Kaufman, Y. J., C. O. Justice, L. P. Flynn, J. D. Kendall, E. M. Prins, L. Giglio, D. E. Ward, W. P. Menzel, and A. W. Setzer (1998b), Potential global fire monitoring from EOS-MODIS, *J. Geophys. Res.*, *103*, 32,215–32,238.

Kirkevag, A., T. Iverson, and A. Dahlback (1999), On radiative effects of black carbon and sulphate aerosols, *Atmos. Environ.*, *33*, 2621–2635.

Korontzi, S., D. P. Roy, C. O. Justice, and D. E. Ward (2004), Modeling and sensitivity analysis of fire emissions in southern Africa during SAFARI 2000, *Remote Sens. Environ.*, *92*, 255–275.

Langaas, S. (1995), A critical review of sub-resolution fire detection techniques and principles using thermal satellite data, Ph.D. thesis, Dep. of Geogr., Univ. of Oslo, Oslo, Norway.

Malamud, B. D., G. Morein, and D. L. Turcotte (1998), Forest fires: An example of self-organised critical behavior, *Science*, *281*, 1840–1841.

Mayaux, P., E. Bartholomé, S. Fritz, and A. Belward (2004), A new land-cover map of Africa for the year 2000, *J. Biogeogr.*, *31*, 861–877.

Moula, M., J. M. Brustet, and J. Fontan (1996), Remote sensing-modelisation approach for diurnal estimation of burnt biomass in the Central African Republic savanna, *J. Atmos. Chem.*, *25*, 1–19.

Pack, D. W., C. J. Rice, B. J. Tressel, C. J. Lee-Wagner, and E. M. Oshika (2000), Civilian uses of military surveillance satellites, *Crosslink*, *1*(1), 2–8.

Pereira, J. M. C., B. Mota, J. L. Privette, K. K. Caylor, J. M. N. Silva, A. C. L. Sa, and W. Ni-Meister (2004), A simulation analysis of the detectability of understory burns in *miombo* woodlands, *Remote Sens. Environ.*, *93*, 296–310.

Prins, E. M., and W. P. Menzel (1994), Trends in South American biomass burning with the GOES visible infrared spin scan radiometer atmospheric sounder from 1983 to 1991, *J. Geophys. Res.*, *99*, 16,719–16,735.

Prins, E. M., J. M. Felts, W. P. Menzel, and D. E. Ward (1998), An overview of GOES-8 diurnal fire and smoke results for SCAR-B and 1995 fire season in South America, *J. Geophys. Res.*, *103*, 31,821–31,835.

Reid, J. S., E. M. Prins, D. L. Westphal, C. C. Schmidt, K. A. Richardson, S. A. Christopher, T. F. Eck, E. A. Reid, C. A. Curtis, and J. P. Hoffman (2004), Real-time monitoring of South American smoke particle emissions and transport using a coupled remote sensing/box-model approach, *Geophys. Res. Lett.*, *31*, L06107, doi:10.1029/2003GL018845.

Riggan, P., R. Tissell, R. Lockwood, J. Brass, J. Pereira, H. Miranda, T. Campos, and R. Higgins (2004), Remote measurement of energy and carbon flux from wildfires in brazil, *Ecol. Appl.*, *14*, 855–872.

Robinson, J. M. (1991), Fire from space: Global fire evaluation using infrared remote sensing, *Int. J. Remote Sens.*, *12*, 3–24.

Roy, D. P., P. E. Lewis, and C. O. Justice (2002), Burned area mapping using multi-temporal moderate spatial resolution data: A bidirectional reflectance model-based expectation approach, *Remote Sens. Environ.*, *83*, 263–286.

Saunders, R. W., and K. T. Kriebel (1988), An improved method for detecting clear sky and cloudy radiances from AVHRR data, *Int. J. Remote Sens.*, *9*, 123–150.

Schmetz, J., P. Pili, S. Tjemkes, D. Just, K. Kerkmann, S. Rota, and A. Ratier (2002), An introduction to Meteosat Second Generation (MSG), *Bull. Am. Meteorol. Soc.*, *83*, 977–992.

Scholes, R. J., J. Kendal, and C. O. Justice (1996), The quantity of biomass burned in southern Africa, *J. Geophys. Res.*, *101*, 23,667–23,676.

Schultz, M. (2002), On the use of ATSR fire count data to estimate the seasonal and interannual variability of vegetation fire emissions, *Atmos. Chem. Phys.*, *2*, 387–395.

Seiler, W., and P. J. Crutzen (1980), Estimates of gross and net fluxes of carbon between the biosphere and the atmosphere from biomass burning, *Climate Change*, *2*, 207–247.

Shea, R. W., B. W. Shea, J. B. Kauffman, D. E. Ward, C. I. Haskins, and M. C. Scholes (1996), Fuel biomass and combustion factors associated with fires in savanna ecosystems of South Africa and Zambia, *J. Geophys. Res.*, *101*, 23,551–23,568.

Silva, J. M. N., J. F. C. L. Cadima, J. M. C. Pereira, and J.-M. Gregoires (2004), Assessing the feasibility of a global model for multi-temporal burned area mapping using SPOT-VEGETATION data, *Int. J. Remote Sens.*, *25*, 4889–4913.

Smith, A. M. S., M. J. Wooster, A. K. Powell, and D. Usher (2002), Texture based feature extraction: Application to burn scar detection in Earth observation satellite sensor imagery, *Int. J. Remote Sens.*, *23*, 1733–1739.

Smith, A. M. S., M. J. Wooster, N. D. Drake, G. L. W. Perry, and F. Dipotso (2005), Fire in African savanna: Testing the impact of incomplete combustion on pyrogenic emissions estimates, *Ecol. Appl.*, *15*, 1074–1082.

Strauss, D., L. Bednar, and R. Mees (1989), Do one percent of forest fires cause ninety-nine percent of the damage?, *For. Sci.*, *35*, 319–328.

Stroppiana, D., J.-M. Gregoire, and J. M. C. Pereira (2003), The use of SPOT VEGETATION data in a classification tree approach for burnt area mapping in Australian savanna, *Int. J. Remote Sens.*, *24*, 2131–2151.

Swap, R. J., H. J. Annegarn, T. Suttles, M. D. King, S. Platnick, J. L. Privette, and R. J. Scholes (2003), Africa burning: A thematic analysis of the Southern African Regional Science Initiative (SAFARI 2000), *J. Geophys. Res.*, *108*(D13), 8465, doi:10.1029/2003JD003747.

Van der Werf, G., R. Randerson, G. J. Collatz, and L. Giglio (2003), Carbon emission from fires in tropical and subtropical ecosystems, *Global Change Biol.*, *9*, 547–562.

Ward, D. E., W. M. Hao, R. A. Susott, R. E. Babbitt, R. W. Shea, J. B. Kauffman, and C. O. Justice (1996), Effect of fuel composition on combustion efficiency and emission factors for African savanna ecosystems, *J. Geophys. Res.*, *101*, 23,569–23,576.

Wittenberg, U., M. Heimann, G. Esser, A. McGuire, and W. Sauf (1998), On the influence of biomass burning on the seasonal CO2 signal as observed at monitoring stations, *Global Biogeochem. Cycles*, *12*, 531–544.

Wolfe, R. E., M. Nishihama, A. J. Fleig, J. A. Kuyper, D. P. Roy, J. C. Storey, and F. S. Patt (2002), Achieving sub-pixel geolocation accuracy in support of MODIS land science, *Remote Sens. Environ.*, *83*, 31–49.

Wooster, M. J., and N. Strub (2002), Study of the 1997 Borneo fires: Quantitative analysis using global area coverage (GAC) satellite data, *Global Biogeochem. Cycles*, *16*(1), 1009, doi:10.1029/2000GB001357.

Wooster, M. J., and Y. H. Zhang (2004), Boreal forest fires burn less intensely in Russia than in North America, *Geophys. Res. Lett.*, *31*, L20505, doi:10.1029/2004GL020805.

Wooster, M. J., B. Zhukov, and D. Oertel (2003), Fire radiative energy for quantitative study of biomass burning: Derivation from the BIRD experimental satellite and comparison to MODIS fire products, *Remote Sens. Environ.*, *86*, 83–107.

Wooster, M. J., G. Perry, B. Zukov, and D. Oertel (2004), Biomass burning emissions inventories: Modelling and remote sensing of fire intensity and

biomass combustion rates, in *Spatial Modelling of the Terrestrial Environment*, edited by R. Kelly, N. Drake, and S. Barr, pp. 175–196, John Wiley, Hoboken, N. J.

Wooster, M. J., G. Roberts, G. L. W. Perry, and Y. J. Kaufman (2005), Retrieval of Biomass combustion rates and totals from fire radiative power observations: 1. FRP derivational and calibration relationships between biomass consumption and fire radiative energy release, *J. Geophys. Res.*, doi:10.1029/2005JD006318, in press.

Zhang, Y.-H., M. J. Wooster, O. Tutubalina, and G. L. W. Perry (2003), Monthly burned area and forest fire carbon emission estimates for the Russian Federation from SPOT VGT, *Remote Sens. Environ.*, *87*, 1–15.

Zhukov, B., K. Briess, E. Lorenz, D. Oertel, and W. Skrbek (2005), Detection and analysis of high-temperature events in the BIRD mission, *Acta Astronaut.*, *56*, 65–71.

F. Dipotso, Research Division, Department of Wildlife and National Parks, Box 17, Kasane, Botswana.

N. Drake, G. L. W. Perry, G. Roberts, and M. J. Wooster, Department of Geography, Kings College London, Strand, London, WC2R 2LS, UK. (martin.wooster@kcl.ac.uk)

L.-M. Rebelo, Department of Geography, University College London, London, WC2H 0AP, UK.

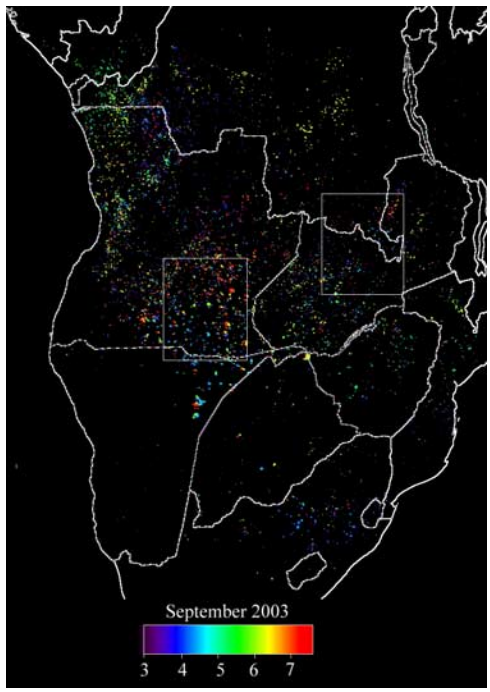

Figure 10. SEVIRI derived spatial distribution and timing of active fires in southern Africa from 1200 UTC on 3 September until 2357 UTC on 7 September 2003. Boxes indicate the 5° × 5° regions whose FRP temporal trends are plotted in Figure 7.